COMPUTATIONAL INVESTIGATIONS ON HYDRODYNAMIC PERFORMANCE OF ACTIVE AND PASSIVE TAILS FOR CARANGIFORM SWIMMERS

Dev Pradeepkumar Nayak

A thesis presented to Lakehead University in fulfilment of the

thesis requirement for the degree of

Master of Science in Mechanical Engineering

Supervisor: Ali Tarokh, PhD, P. Eng

Co-Supervisor: Muhammad Saif Ullah Khalid, PhD, P.Eng

November 17, 2025

Thunder Bay, Ontario, Canada

ABSTRACT

Fish achieve efficient propulsion through their unique capabilities to undulate their bodies for locomotion, and carangiform swimmers are often associated with producing thrust from their rear through their caudal fin. The undulatory kinematics of the caudal fin closely resemble flapping-like behavior composed of heaving and pitching. In this study, we investigate the interaction between the caudal fin and the rest of the swimmer's body through numerical simulations of fluid–structure interaction, segregated into a Two-dimensional and a Three-dimensional study. In the first part, the body and tail are modeled with NACA=0015 and NACA-0012, respectively, at two Reynolds Numbers, 500 and 5000, corresponding to a small and a large fish. The passive pitching of the tail is modeled with a linear torsional spring and a damper at its peduncle. This analysis reveals that a swimmer with a passive pitching tail does not necessarily produce higher thrust compared to its active counterpart but can achieve higher power savings. It also shows that smaller fishes can benefit from a passively pitching tail, whereas larger fishes require an actively pitching tail for optimal performance. In the second part, we extend the work to a three dimensional analysis with an actual model of a Jackfish, where we separate the caudal fin from the swimmer and examine the performance of passively pitching versus active pitching. Here, the passive pitching is modeled with a nonlinear spring to incorporate the stabilizing effect at larger amplitudes, and the study is conducted at a Reynolds Number of 3000. We find that the nonlinear spring enables larger amplitude pitching and that the passively pitching tail produces higher thrust than the actively pitching tail. Overall, the study shows that a nonlinear spring is essential for enforcing large amplitude pitching of the caudal fin which benefits the swimmer to generate higher thrust, while with a linear spring and smaller pitching amplitudes, locomotion involves a trade-off where the

swimmer prioritizes thrust production or power savings.

I hereby declare that I am the sole author of this thesis.

Dev Pradeepkumar Nayak

I authorize Lakehead University to lend this thesis to other institutions or individuals for the purpose of scholarly research.

Dev Pradeepkumar Nayak

I further authorize Lakehead University to reproduce this thesis by photocopying or by other means, in total or in part, at the request of other institutions or individuals for the purpose of scholarly research.

Dev Pradeepkumar Nayak

Dedication

To my beloved parents,

*હું આ કાર્ય મારા માતા-પિતા, **Nina Nayak** અને **Pradeep Nayak**, ને સમર્પિત કરું છું, જેમણે મને બધું આપ્યું છે. તેમનો અડગ પ્રેમ, સહારો અને મારા પરનો વિશ્વાસે શંકાના ક્ષણોમાં મને આગળ વધાર્યો છે અને મુશ્કેલ સમય દરમિયાન મને મજબૂત બનાવ્યો છે. સારો ભવિષ્ય ઊભું કરી શકું તે માટે તેમણે મને ઘરથી દૂર મોકલ્યો, આ ત્યાગનો ઋણ હું ક્યારેય સંપૂર્ણ રીતે ચૂકવી શકીશ નહીં. આ થિસિસ મારી કૃતજ્ઞતાનું નમ્ર અર્પણ છે, અને ભવિષ્યમાં તેમની સાથે વહેંચવા ઇચ્છતા અનેક સિદ્ધિઓ તરફનું એક નાનું પગલું છે.*
હું તમને પ્રેમ કરું છું, મા અને પપ્પા.

*(I dedicate this work to my parents, **Nina Nayak** and **Pradeep Nayak**, who have given me everything. Their unwavering love, support, and belief in me have carried me through moments of doubt and strengthened me during challenging times. Their sacrifice in sending me far from home so I could build a better future is something I can never fully repay. This thesis is a humble offering of gratitude, a small step toward the many achievements I hope to share with them.*

I love you, Mom and Dad.)

Acknowledgments

I would like to express my deepest gratitude to my supervisor, **Dr. Ali Tarokh**, for his mentorship from my undergraduate project throughout the duration of this research. His insightful feedback and constant support have shaped not only the direction of this work but also my growth as an independent researcher. I am especially thankful for his confidence in my abilities and for providing me with the opportunity to begin my career as a researcher. Working under his supervision has been both an honor and a transformative learning experience.

I would also like to extend my sincere appreciation to my co-supervisor, **Dr. Muhammad Saif Ullah Khalid**, who trusted me to work on this research, which is very dear to him. His insight into the field, valuable guidance, constructive suggestions, and technical expertise greatly enriched this study. I am grateful for his consistent support, timely feedback, and the many discussions that helped refine the ideas presented in this thesis. His mentorship has significantly contributed to my academic and professional development.

I am sincerely grateful to my thesis committee members, **Dr. Leila Pakzad** and **Dr. Kefu Liu**, for their time, constructive feedback, and valuable insights, which have greatly contributed to the refinement and improvement of this research.

I cannot overstate the emotional support I have received from my parents, **Mrs. Nina Pradeep-**

kumar Nayak and **Mr. Pradeepkumar Khodidas Nayak**, and my sisters, **Mrs. Nupur Kulbhushan Nayak** and **Mrs. Jhanvi Nisarg Gandhi**. I am also thankful to my brothers-in-law, **Dr. Kulbhushan Nayak** and **Dr. Nisarg Gandhi**, for their support throughout the duration of my research. Without their unwavering encouragement, this work would not have been possible. I further extend my appreciation to my girlfriend, **Ms. Madeline Emilee Coppock**, who stood by my side throughout this journey and supported me during the most challenging times.

I also extend my sincere appreciation to my dear friends **Dev Patel**, **Kaizerin**, **Dilip**, **Aishwarya**, and **Harvi**, who always had my back during the most difficult moments of this research journey.

I further extend my appreciation to **Mr. Kamlesh Navlani**, who sparked my passion for pursuing a career in engineering. I would also like to thank my colleagues and peers who supported me during challenging times in my master's program and made the lab feel like home: **Faisal Muhammad**, **Amirhossein Fardi**, **Maham Kamran**, **Hao Wang**, **Zahra Maleksabet**, **Aysan Gholami**, **Soorena Azarhazin**, and **Maryum Waseem**.

I sincerely acknowledge the financial and computational support provided by NSERC, the Digital Research Alliance of Canada, and Lakehead University. Their funding and resources were crucial to the successful completion of this research.

I offer my humble thanks to **Goddess Shakti**, whose blessings, strength, and protection have guided me through the challenges of this research.

Contents

Abstract

Declaration

Dedication

Acknowledgments

Contents

List of Figures

List of Tables

1 Introduction **1**

2 Numerical Methodology **6**

2.1 Kinematic Modes 6

2.1.1 Kinematics of the swimmer in 2D 8

2.1.2 Geometry and kinematics of Jackfish 10

2.2 Flow domain 13

2.2.1 Flow domain and geometry for the swimmer in 2D 14

2.2.2 Flow domain and geometry for the swimmer in 3D 15

2.3 Verification and validation study 16

2.3.1 Two-Dimensional verification 16

2.3.2 Three-Dimensional verification 20

3 2D Investigations of Caudal Fins of Carangiform Swimmers 23

3.1 Quantitative analysis on actively pitching tail 23

3.2 Quantitative analysis on passively pitching tail 28

3.3 Comparative Vortex Dynamics of Active and Passive Pitching Tails 35

4 3D Investigations of Caudal Fins of Carangiform Swimmers 46

4.1 Summary 69

4.2 Conclusions 70

4.3 Recommendations for Future Work 72

Bibliography 74

List of Figures

1.1 Medial view of a Jackfish and its superior view for its $2D$ Kinematics. 2

2.1 Two-dimensional model of the fish at (a) static position ($t/\tau = 0$), and (b) mid-oscillation instant ($t/\tau = 0.55$). 8

2.2 Two-dimensional model of the fish at (a) static position ($t/\tau = 0$), and (b) mid-oscillation instant ($t/\tau = 0.55$). 11

2.3 Flow domain and boundary conditions. 16

2.4 Flow domain and boundary conditions. 17

2.5 Results for convergence of Grid size. 18

2.6 Results for convergence of Time step. 19

2.7 Comparison of our results (a) C_T, and (b) C_L with those of Gao et al (1). 20

2.8 Results for convergence of Grid size.Pot with $Q = 40$ with the y-vorticity shows the iso-surface for (a) the coarse grid, (b) medium grid, and (c) fine grid. The Drag coefficient (C_D), and (d), and Lift coefficient (C_L) is plotted for all three grids for grid convergence analysis. 21

2.9 Flow domain and boundary conditions. 22

3.1 Model of the actively pitching tail mimicking a swimmer with continuous undulatory flexure. 25

3.2 Stability map (a)-(f) insets illustrate C_D for a typical stable (g) and unstable (h) cases. 28

3.3 Mean drag coefficient of the passively pitching tail at (a) Re = 500, and (b) 5000. . 30

3.4 Power ratio at (a) Re = 500, and (b) 5000. 34

3.5 Vorticity contours corresponding to the swimmer with (a-e) an actively pitching tail, and (f-j) a passively pitching tail respectively at Re = 500. 37

3.6 Vorticity contours corresponding to the swimmer with (a-e) an actively pitching tail, and (f-j) a passively pitching tail respectively at Re = 5000. 38

3.7 Vortex dynamics of actively and passively pitching tails at Re 500 and $f^* = 0.6$. Panels (a) and (b) show the variations of force coefficients C_D, C_L, and C_M over one oscillation cycle for the actively and passively pitching tails, respectively. Panels (c) and (d) depict four characteristic snapshots (1-4) of the flow field for each case, respectively, visualized using contours of z-vorticity corresponding to the same cycle. 40

3.8 Vortex dynamics of actively and passively pitching tails at Re 5000 and $f^* = 0.2$. Panels (a) and (b) depict four characteristic snapshots (1-4) of the flow field for each case, respectively, visualized using contours of z-vorticity corresponding to a half oscillation cycle. 42

3.9 Fast Fourier Transform (FFT) of the pitching response of the tail at (a) Re = 500, $f^* = 0.6$, $J^* = 0.125$ & $\zeta = 1.0$, and (b) Re = 5000, $f^* = 0.2$. $J^* = 0.375$, & $\zeta = 0.5$ 45

4.1 Synchronous and asynchronous map for the passively pitching tail with a nonlinear stiffness. 48

4.2 The plot shows the (a) cycle-by-cycle pitching frequency of the caudal fin for ζ = 0.300-0.450 with its corresponding tuning parameter n. And the (b) deviation of the frequency to its preceding cycle till it reaches stablility. 50

4.3 Amplitude envelope of carangiform swimmer with (a) undulatory trajectory of the caudal fin alongside its pitching trajectory. (b) represents the active pitching trajectory of the caudal fin over a full oscillation cycle 51

4.4 Schematic of Jackfish used to represent the pitching of the caudal fin in this study. . 52

4.5 Pitching displacement of the caudal fin over a full oscillation cycle for the passively pitching tail alongside its active counterpart. 52

4.6 Wake signature for all of the configurations from a dorsal view. for (a) an actively pitching tail, alongside (b)-(h) the passively pitching tail for case 4 to 10, respectively. 54

4.7 Schematic of the case 10 at different stages of its full oscillation cycle. 55

4.8 The comparison of the heaving and pitching of the caudal fin for (a) passively pitching tail with ζ = 0.367 and n = 50, and ζ = 0.433 and n = 58 corresponding to case 5, and case 9, respectively. And, (b) Actively pitching tail 56

4.9 Schematic of the (1a)-(1e) case 5, and (2a)-(2e) case9 9 at different stages of its full oscillation cycle. In comparison with the schematic of the actively pitching case in black. 57

4.10 (a) Moment coefficient (C_M), and (b) Drag coefficient (C_D) Comparison between the case 5, case 9, and the actively pitching tail over an oscillation cycle. 59

4.11 Nomenclature used to track the vortices developed and sheded from the caudal fin of the Jackfish 60

4.12 Plot showing the closeup vortices generated and sheded in a half oscillation cycle (a)-(f)from the caudal fin of the Jackfish for case 5. Plot shows the iso-surface of $Q = 40$ colored by the range of y-vorticity. 61

4.13 This figure presents the ring vortex generated in case 5 at $t/\tau = 0.6$, shown from (a) the dorsal view and (b) the isometric view. Image (c) indicates the locations of the iso-surface slices along the z-axis from the anterior view of the swimmer, corresponding to images (d)–(f), which display the streamwise velocity contours extracted from each slice. 63

4.14 y-Vorticity contours corresponding to the swimmer from the dorsal view at the end of an oscillation cycle for (a) case with an actively pitching tail, (b) case 5, and (c) case 9. Plot shows the iso-surfaces at $Q = 40$, and translucent $Q = 8$. 65

4.15 x-Vorticity contours corresponding to the swimmer from the (a) iso-matric view, and (b) the dorsal view at the end of an oscillation cycle with the iso-surfaces at $Q = 40$, and translucent $Q = 8$ 66

4.16 Iso-surface shows the cycle-averaged value for the case with ($a1$ & $a2$) an actively pitching tail, ($b1$ & $b2$) case 5, and ($c1$ & $c2$) case 9 referring to $\overline{U_{xmax}}$, $\overline{U_{xmin}}$, respectively. 67

List of Tables

2.1 Geometric quantities of the Jack fish model with an independent caudal fin as a rigid body (All the quantities are normalized using by L). 11

2.2 Specifications of governing parameters for simulation methodology 19

2.3 Mesh refinement details between coarse, medium, and fine grids. Refinement (I) denotes the comparison between Coarse and Medium, while Refinement (II) denotes the comparison between Medium and Fine. 22

3.1 Specifications of governing parameters for 2D analysis 24

3.2 Time-averaged power coefficients and power ratio (η) of the actively pitching tail at Re = 500 and Re = 5000. 26

3.3 Time-averaged drag coefficients of the actively pitching tail at Re = 500 and Re = 5000. 27

3.4 Data on stable cases presenting the mean drag coefficient ($\overline{C_D}$) and maximum pitching angle ($\theta_{p,\max}$) of the passively pitching tail across Strouhal frequencies (f^*), damping ratios (ζ), and inertia ratios (J^*) at Reynolds numbers Re = 500 and Re = 5000. 32

4.1 Specifications of governing parameters for 3D analysis. 47

4.2 Range of mode-5 synchronous analysis for the pitching of the caudal fin 49

Chapter 1

Introduction

Nature has long served as a source of inspiration for engineering innovation, opening pathways to previously unexplored technologies. Aquatic organisms, in particular, display an extraordinary combination of maneuverability, control, efficiency, adaptability, and speed—qualities that motivate the development of advanced robotic systems in both aerial and underwater domains. Through millions of years of evolution and natural selection, fish have refined their swimming strategies to operate with outstanding hydrodynamic efficiency, using undulatory kinematics that enable effective propulsion and agile maneuvering. The interaction between fish bodies and their surrounding fluid environment has been widely investigated through experimental studies (2–5) and computational fluid dynamics (CFD) simulations (6–8).

The efficiency of fish locomotion emerges from sophisticated fin–body coordination and the controlled generation of vortical structures that improves thrust and maneuverability. This has led to a growing field of biomimetic propulsion research. The importance of such investigations is amplified by the increasing challenges facing marine ecosystems, including climate change and pollution (9). Understanding the adaptive locomotion strategies of fish not only informs biology

but directly contributes to the advancement of autonomous underwater vehicles (AUVs) (3; 10–12). Recent studies have shown that underwater sensing, such as odor detection in turbulent wakes, can guide biomimetic navigation strategies (13), while deep learning integrated with immersed-boundary–lattice–Boltzmann frameworks has improved our understanding of complex swimming behaviors such as Kármán gaiting and prey capture (14).

Among aquatic swimmers, carangiform species are of particular interest due to their distinctive locomotion style. Their undulatory kinematics are concentrated toward the posterior end, with large lateral displacements near the peduncle and caudal fin. Numerous studies have highlighted the crucial influence of peduncle shape and caudal fin morphology on propulsion (15; 16). As illustrated in Fig. 1.1, the amplitude envelope of a Jackfish demonstrates how displacement intensifies toward the tail, reinforcing its dominant role in thrust production.

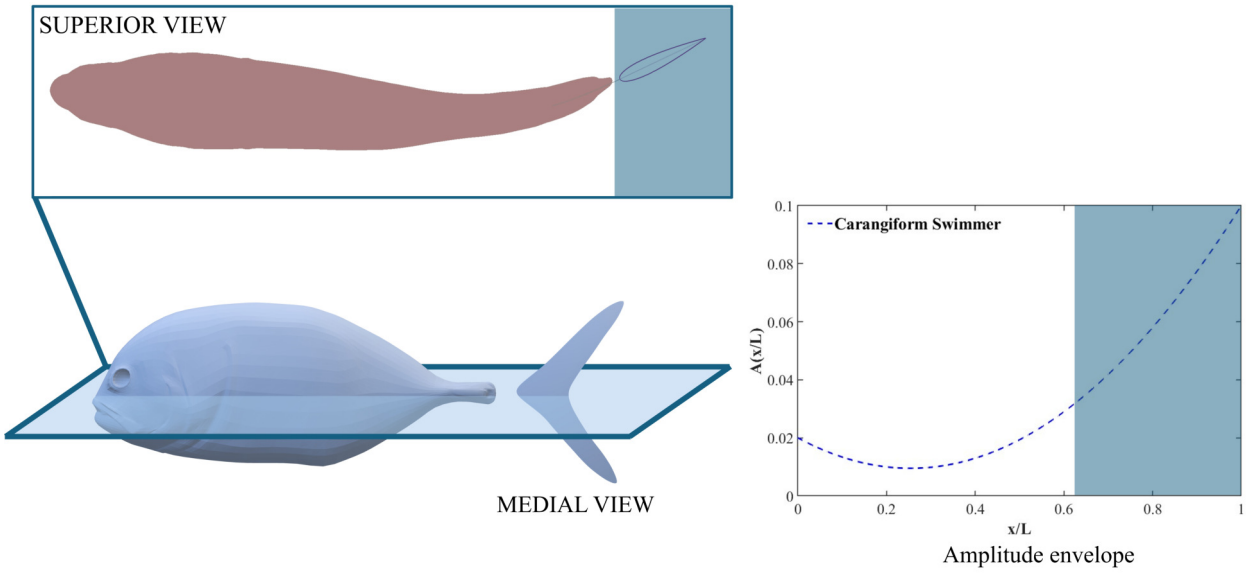

Figure 1.1: Medial view of a Jackfish and its superior view for its 2*D* Kinematics.

The caudal fin in carangiform swimmers acts as the primary contributor to thrust. Its kinematics can be interpreted as a coupled heaving–pitching motion that aligns with classical flapping-foil

theory (17). The relationship between flapping motions and thrust generation dates back to the foundational work of Knoller and Betz (18; 19). The tail beat sheds vortices of high propulsive efficiency (20), and evolutionary adaptation has produced a robust peduncle capable of transmitting muscular and elastic energy to the fin effectively (21).

In both experimental and numerical studies, passive foils have been shown to serve as powerful analogues for freely swimming fish through their ability to self-propel using fluid–structure interaction (22–24). Lauder et al. (22) demonstrated that even when stiffness is held constant, trailing-edge geometry alone can substantially alter swimming speed, emphasizing the role of morphological diversity in fin evolution. Similarly, Liu et al. (25) used coupled fluid-structure solvers to determine how real fins deform and contribute to thrust, while Hang et al. (16) showed that passive bending near the posterior region can favor swimming economy despite limitations in maximum speed.

Beyond propulsion, fins act as crucial control surfaces. Fish and Lauder (26) highlighted how fins integrate active muscle-driven actuation with passive structural response to support stability and maneuverability. This paradigm has inspired numerous robotic designs. Behbahani et al. (27) developed a passive feathering joint that cuts drag during the recovery stroke; Qiu et al. (28) proposed a tendon-driven robotic fish with a passively deflecting variable-stiffness fin; Chen et al. (29) introduced compliant torsional joints for multi-segment swimmers; and Wang et al. (30) produced a modular variable-stiffness passive joint that adaptively improves performance. Lu et al. (31) further showed that hybrid active–passive fin-ray designs can drastically enhance thrust generation.

Across these works, a consistent theme emerges: passive joints between the body and fin amplifies the swimming performance, yet the fundamental fluid dynamic mechanisms responsible

for these improvements remain incompletely resolved. Importantly, the connection between the peduncle and caudal fin is frequently modeled using nonlinear stiffness, particularly cubic nonlinear terms which allow the fin to amplify displacement near mid-stroke and exhibit a recoil-type restoring motion at large deflections (31–33). This nonlinear behavior supports synchronized locomotion, but the vortex interactions between the body and the fin associated with such passive pitching remain poorly understood.

Motivated by this gap, the present study investigates the hydrodynamic performance of a carangiform swimmer comprising an undulating body and a passively pitching tail dynamically modelled by a torsional spring. Using a NACA-0015, and NACA-0012 for thew body and tail (1), for the two-dimensional analysis with Re = 500, and 5000. A Jackfish-inspired morphology in three-dimensional analysis, with the similar streamwise length that of the geometry in the two diensional studywe employ an FSI-based framework in `OpenFOAM` v2312 to solve the Navier–Stokes equations at a Reynolds number of Re = 3000. In the first part of the analysis in $2D$ we uncorporate the passive pitching of the caudal fin using a linear tosional spring, and a damper. For the second half of the study in $3D$ we extend the analysis to a use of nonlinear spring in the system to add stability at larger amplitudes. The objectives of this thesis are to: (*i*) investigate the performance of a passively pitching tail with a linear peduncle spring in $2D$, (*ii*) examine how damping, Stouhal frequency, and Inertia influences the synchronization between passive pitching and the undulation of the body, (*iii*) compare the hydrodynamic performance of passive and active pitching mechanisms, and (*iv*) elucidate the vortex interactions between the swimmer and the fluid that contributes to thrust. (*v*) Analyze the passive pitching with a nonlinear spring and its influence on the formation of vortical structures contributing to thrust. By addressing these questions, this work provides new insight into the functional role of nonlinear passive pitching of the caudal fin in biological

swimmers and establishes guiding principles for the development of next-generation bio-inspired underwater robotic platforms.

Chapter 2

Numerical Methodology

In the present study, the flow over the swimmer is investigated through two-dimensional and three-dimensional analyses at a lower Reynolds number. This chapter outlines the numerical methodology employed in the current work. All numerical simulations are conducted using OpenFOAM 2312, where the finite volume method with second-order discretization schemes is utilized to solve the governing equations. The incompressible continuity and Navier–Stokes equations, derived from the fundamental principles of conservation of mass and momentum, are presented in this section. Furthermore, the solver and the methodologies adopted in this study have been validated extensively, and the proof of the numerical approach is shown in this chapter.

2.1 Kinematic Modes

For this study, we model the swimmer using an undulatory profile characteristic of a carangiform swimmer. To conduct a detailed analysis of the kinematics of the tail (caudal fin), the body (trunk) of the swimmer is modelled separately. The displacement of the carangiform undulation (13; 34–

36) defined by the following equation.

$$A\left(\frac{x}{L}\right) = 0.02 - 0.085\left(\frac{x}{L}\right) + 0.1625\left(\frac{x}{L}\right)^2; \quad 0 < \frac{x}{L} < c_b \tag{2.1}$$

$$y\left(\frac{x}{L}\right) = f\,(t)\; A\left(\frac{x}{L}\right)\cos\left[2\pi\left(\frac{xL}{\lambda} - ft\right)\right] \tag{2.2}$$

$$f\,(t) = \left[\frac{e^{3t} - 1}{e^{3t} + 1}\right] \tag{2.3}$$

Where $A(x/L)$ represents the local amplitude and $y(x/L)$ represents the displacement envelope over the body of the swimmer, f represents the undulatory frequency, and λ represents the wavelength of the swimmer which is set to $\lambda = 1$ for this study. The rear of the swimmer is modeled with flapping kinematics. The heaving of the tail is modeled as a (h) of the virtual joint at its peduncle, $h = A(0.78)$. The oscillating motion and the undulating motion is modeled by the mathematical expression, as presented as Eq. 2.2. The motion of the body and tail is initiated using a hyperbolic tangent function (also referred to as a Sigmoid function), given in Eq. 2.3, to ensure a smooth transition to the peak amplitude of undulation, active heaving, and active pitching. In this formulation, the exponent is cubed to produce a faster yet smoother rise to the peak amplitude. Notably, applying the Sigmoid function enables the passively pitching tail to reach steady-state oscillation much faster than without it, thereby reducing the overall computational cost.

For the subsequent analysis, the body (trunk) and the tail (caudal fin) of the swimmer are modeled using two different geometries for the two-dimensional and three-dimensional studies, respectively. The total length of the swimmer is kept constant in the streamwise direction and set

to $L = 1$, which is used to normalize all other length-related parameters. The undulatory body of the swimmer is $0.75L$, while the independent tail has a length of $0.20L$. These two components are connected through a virtual joint located at the peduncle, incorporating a torsional spring and a damper. A small gap of $0.05L$ is maintained between the main body and the tail to allow for the interaction at the joint inspired from the work proposed by Gao et al. (1).

2.1.1 Kinematics of the swimmer in 2D

We model the swimmer in our $2D$ analysis which represents a section of a model of the fish from its dorsal view. We keep a small gap between the swimmer and the tail to model the tail as an independently pitching tail. Here, the tail pitches about its peduncle, situated between the body and the tal.

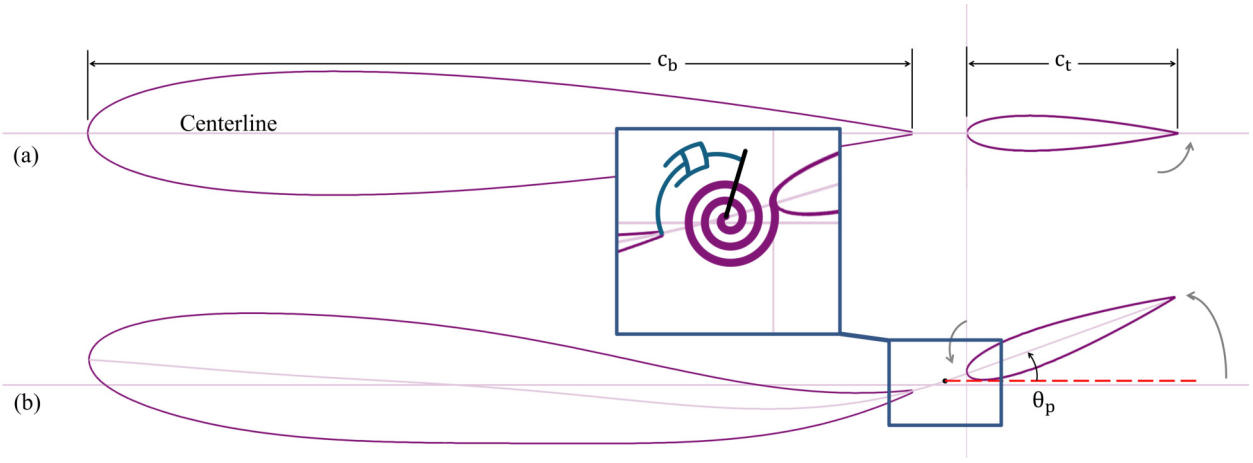

Figure 2.1: Two-dimensional model of the fish at (a) static position ($t/\tau = 0$), and (b) mid-oscillation instant ($t/\tau = 0.55$).

Figure. 2.1 shows the modeled flexure of the undulating body with a passively pitching tail in $2D$. We model the body and tail of a carangiform-like swimmer by using two foils. The body modeled using a NACA-0015 foil is set to $c_b = 0.75L$, and length of the tail using a NACA-0012

foil is set up, respectively, (see Fig.2.1), following the geometric features presented by by Gao et al, (1)The tail is attached to the body using a torsional spring and a viscous damper at the peduncle as illustrated in Fig. 2.1b. As the undulation begins, the body and the tail follow the trajectory as shown in Fig. 2.1b, where θ_p is the pitching angle that the tail makes with the centerline of the whole body when it is straight and stationary. The dashed line in Fig. 2.1b shows the location of peduncle. The pitching dynamics of the tail is governed by the following equation:

$$\left[\frac{2\,c_t^2}{U_\infty^2}\,J^*\right]\ddot{\theta}_p + \left[\frac{2\,c_t}{U_\infty}\,C^*\right]\dot{\theta}_p + [2\,K^*]\,\theta_p = C_M \tag{2.4}$$

$$J^* = \frac{J_\theta}{\rho\, s\, c_t^4},\ K^* = \frac{K_\theta}{\rho\, U_\infty^2\, s\, c_t^2},\ C^* = \frac{c_\theta}{\rho\, U_\infty\, s\, c_t^3},\ C_M = \frac{2M}{\rho\, U_\infty^2\, s\, c_t^2}.$$

Where, ρ denotes density of the fluid; U_∞, the freestream velocity, s the span of the tail in the lateral (out-of-plane) direction (chosen as unity in this study); M the hydrodynamic moment about the pitching axis (pitching about the peduncle); J_θ the mass moment of inertia about the pitching axis. Besides, c_θ and K_θ represent the torsional damping coefficient and stiffness of the body-tail joint, respectively. The dimensionless stiffness coefficient (K^*) is set as a dependent variable on dimensionless Inertia (J^*) as explained below in Eq. 2.5.

$$K^* = J^*\left[\frac{\pi\, n\, c_t\, f^*}{a}\right]^2 \tag{2.5}$$

$$f^* = \frac{2af}{U_\infty} \tag{2.6}$$

In Eqs. 2.5, and 2.6, a is the tail-beat amplitude of the body at $x/L = 0.75$, and f is the frequency at which the body undulates. Here, n represents the n^{th} multiple of the natural frequency

which triggers the super-harmonic resonance of the system and is also referred as a tuning parameter in this study and contributes towards the dominating frequency, resulting in pitching of the tail at the same frequency as that of the heaving (For this Chapter. 2.3.2, $n = 10$) (37; 38). Determined based on several test simulations performed with different values of n. In Chapter. 2.3.2 $n = 10$ exhibits the best tuning between the undulating body and heaving, and independently pitching tail. The normalized damping coefficient (C^*) is determined by the damping ratio (ζ), and dimensionless stiffness coefficient (K^*) (24), according to Eq. 2.7.

$$C^* = 2\,\zeta\,\sqrt{J^* K^*} \tag{2.7}$$

2.1.2 Geometry and kinematics of Jackfish

We model the geometry of the Jackfish and its kinematics similar to that of reported by Liu et al. (39) and .(35). We modify the geometry to construct the model with an independent caudal fin which is connected to the trunk of the Jackfish. we model the Jack Fish without the dorsal fin and the anal fin. Both the trunk and the caudal fin are scaled down by 13% to ensure that the total length of the Jack Fish remains $1L$, and the gap between the Trunk and Caudal fin is at $c_{pe} = 0.05L$ as shown in Fig. 2.2. The gap between the trunk and the caudal fin alongside the length of the trunk ($c_{Tr} = 0.75L$), and the caudal fin ($c_{Ca} = 0.20L$) is chosen as reported by Gao et al. (1).

Figure. 2.2 shows the modeled flexure of the trunk with a passively pitching caudal fin. The caudal fin is attached to the truck via a torsional spring and a viscous damper at the peduncle as illustrated in Fig. 2.2b. Fig. 2.2b, and 2.2c shows the important parametric quantities crucial for this study. Refer to table. 2.1 for the normalized parameters specified for the geometry. Here the

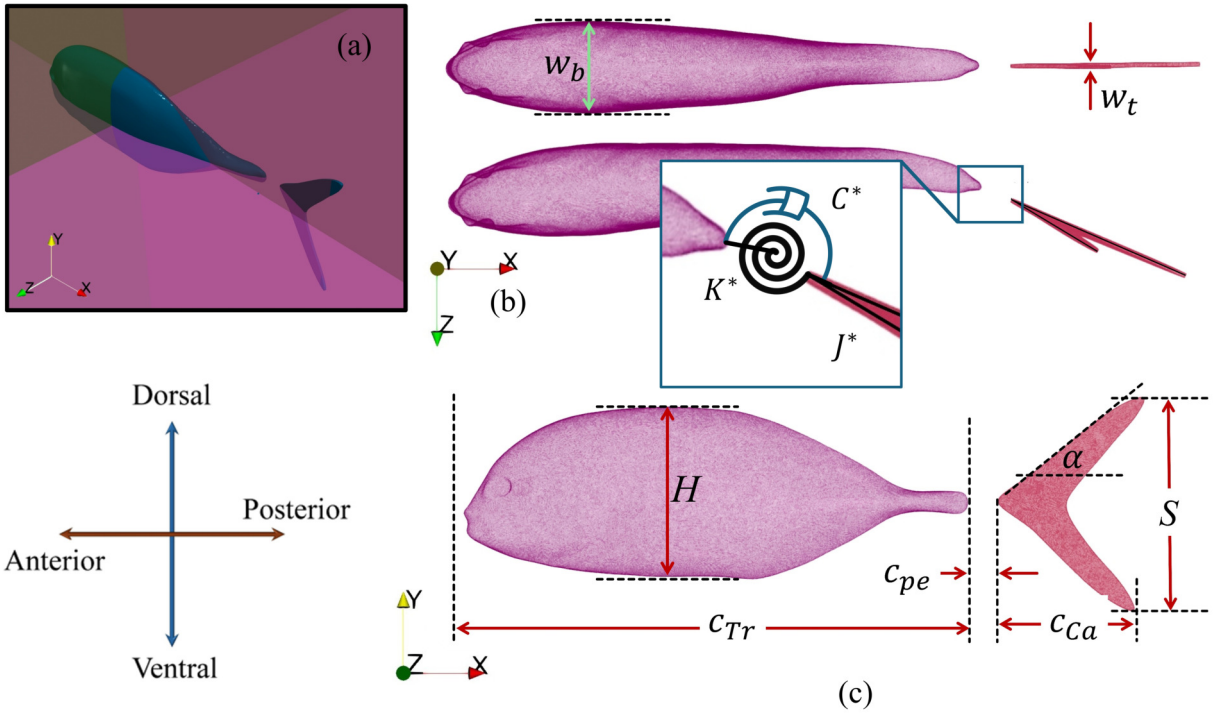

Figure 2.2: Two-dimensional model of the fish at (a) static position ($t/\tau = 0$), and (b) mid-oscillation instant ($t/\tau = 0.55$).

reference area of the caudal fin is calculated based on the AR based on the trailing edge span of the caudal fin S as epr the relationship $AR = S^2/A_{CF}$, where the A_{CF} refers to the area of the caudal fin

C_{Tr}	C_{pe}	C_{Ca}	$\alpha(Deg)$	S	AR	W_b	w_t
$0.75L$	$0.05L$	$0.20L$	40	$0.295L$	4.31	$0.12L$	$0.005L$

Table 2.1: Geometric quantities of the Jack fish model with an independent caudal fin as a rigid body (All the quantities are normalized using by L).

The passive pitching of the caudal fin is modeled using a nonlinear torsional spring inspired by the stiffness-modulation mechanisms observed in biological peduncles. As demonstrated by Lu et al. (32), the musculature and tendon structures in the caudal peduncle do not behave as linear elastic

elements; instead, they exhibit a displacement-dependent stiffness in which the restoring moment grows disproportionately at larger deflections. This nonlinear behavior allows real swimmers to sustain large pitching amplitudes while stabilizing the fin near its extremes through a recoil-type response generated by the increased stiffness. Following this principle, we incorporate a cubic nonlinear term into the torsional spring model. The linear term contributes to amplifying the pitching amplitude around the neutral position, while the cubic term acts as a stabilizing mechanism that limits excessive rotation by increasing the restoring torque at large angular excursions. This combination reproduces the characteristic "soft-near-neutral, stiff-near-extremes" behaviour associated with nonlinear peduncle dynamics and supports synchronized flapping motion. The resulting passive pitching dynamics of the caudal fin are governed by the following equation (Eq. 2.8).

$$\left[\frac{2\,c_t^2}{U_\infty^2}\,J^*\right]\ddot{\theta}_p + \left[\frac{2\,c_t}{U_\infty}\,C^*\right]\dot{\theta}_p - [2\,K^*]\,(A\theta_p - B\theta_p^3) = C_M \tag{2.8}$$

$$J^* = \frac{J_\theta}{\rho\,A_{ref}\,c_t^3},\ K^* = \frac{K_\theta}{\rho\,U_\infty^2\,A_{ref}\,c_t},\ C^* = \frac{c_\theta}{\rho\,U_\infty\,A_{ref}\,c_t^2},\ C_M = \frac{2M}{\rho\,U_\infty^2\,A_{ref}\,c_t}$$

Where, ρ denotes the fluid density, U_∞ is the freestream velocity. The term M represents the hydrodynamic moment acting about the pitching axis located at the peduncle, while J_θ is the mass moment of inertia about this axis. The coefficients c_θ and K_θ correspond to the torsional damping and torsional stiffness of the body–tail joint, respectively. The parameters A and B describe the relative contributions of the linear and nonlinear components of the torsional stiffness. They satisfy the constraint $A + B = 1$, such that the restoring moment $K_\theta(A\theta_p - B\theta_p^3)$ represents a distributed combination of linear ($A\theta_p$) and cubic nonlinear ($B\theta_p^3$) stiffness. This formulation allows the joint to behave as a soft spring near the neutral position while providing increasing resistance

at larger angular deflections, consistent with nonlinear peduncle mechanics observed in biological swimmers. The dimensionless stiffness coefficient K is treated as a dependent variable that varies with the dimensionless inertia J, as detailed in Eq. 2.5. This coupling allows the model to capture the interplay between geometric inertia, joint stiffness, and the passive pitching dynamics of the caudal fin.

In Eqs. 2.5 and 2.6, a denotes the tail-beat amplitude of the body measured at $x/L = 1.0$ for this part of the analysis, and f is the frequency of undulation of the swimmer. The parameter n can be referred as a synchronizing parameter to tune the pitching of the caudal fin with the active heaving for incorporating the flapping motion of the caudal fin (37; 38). For this study we have performed a set of simulations whith the different values of n as discussed earlier alongside a range of values selected for the ζ. The dimensionless damping coefficient C is determined from the damping ratio ζ and the dimensionless stiffness K according to Eq. 2.7, following the standard formulation for nonlinear oscillators (24).

2.2 Flow domain

For the current research, we use OpenFoam/v2312 which is an open source CDF solver which offers variety of numerical techniques to compute different terms in the governing equations for the fluid flows. Hence, we directly solve the unsteady Navier-Stokes equations for the two-dimensional and three-dimensional fluid flows around the swimmer. The two dimensional study provides the basis for the analysis of the three dimensional research. For the two dimensional analysis we conduct 150 independent simulations with a passively pitching tail and 10 simulations for the actively pitching tail which is used as a reference to evaluate the performance parameters of the

swimmer with a passively pitching tail. The basis established with the two dimensional analysis creates a foundation to extend the work in $3D$ where we perform total 40 simulations with the variation in ζ, and n. With different numerical models and CFD tools for $2D$ and $3D$ we conduct direct numerical simualtions (DNS) of the swimmers. The mathematical model for the fluid flow is based on the following non-dimensional forms of the continuity and incompressible Navier-Stokes equations (13; 36).

$$\frac{\partial u_j}{\partial x_j} = 0 \tag{2.9}$$

$$\frac{\partial u_i}{\partial t} + \frac{\partial}{\partial x_j}\left(u_i u_j\right) = -\frac{1}{\rho}\frac{\partial p}{\partial x_i} + \nu\frac{\partial^2 u_i}{\partial x_j \partial x_j} \tag{2.10}$$

Where $i, j = 1, 2$, the u_i and u_j are the Cartesian components of the flow velocity, p is the pressure, and ρ is the density of the fluid. The temporal term in the governing equations are discretized by using an implicit backward difference scheme. The $PIMPLE$ algorithm is used to couple the pressure and velocity field in an iterative manner over the moving mesh. This algorithm combines the Pressure-Implicit with Splitting of Operators ($PISO$) algorithm and Semi-Implicit Method for Pressure-Linked Equations ($SIMPLE$) algorithm. The convergence criterion for the iterative solution at each time step is set to 10^{-04}. In this study, a Laplace equation with inverse-distance diffusivity is used for dynamic meshing (40).

2.2.1 Flow domain and geometry for the swimmer in 2D

An unstructured grid with a rectangular computational domain is used in this study. The grid illustrated in Fig. 2.3 have boundaries selected to ensure minimal numerical errors. The velocity-

inlet is at a distance of $5L$ from the leading edge of the body LE_b, and the pressure-outlet is set at a distance of $14L$ from the trailing edge of the tail (TE_t). In the downstream direction from LE_b there is a refinement region of length $6L$ to capture the vortical flow features in the wake. The top and bottom boundaries are placed at a distance of $7L$ from the centerline. A uniform velocity field U_∞ is set at the inlet, and the gauge pressure at the outlet, top and the bottom is set to zero (zero Gradient). OpenFoam is a Finite Volume Method (FVM) based solver which requires the $3D$ cells, but the front and back planes are defined as empty for $2D$ simulations(no interpolation in normal direction to the domain).

The computational grid deforms at every time step by solving a Laplacian displacement equation, $\nabla \cdot (\gamma \nabla \xi) = 0$. An inverse-distance diffusivity ($\gamma = 1/d$) referenced the body and tail enforces near-rigid motion close to the foils which smoothly dissipates away from foils. The dimensions of the grid are selected to also ensure that there are enough cells between the boundaries of the domain and the body itself to accommodate the moving mesh.

2.2.2 Flow domain and geometry for the swimmer in 3D

An unstructured grid with a three-dimensional cuboid domain is used in this analysis. The grid illustrated in Fig. 2.4 have boundaries selected to ensure minimal numerical errors. The computational grid deforms at every time step by solving a Laplacian displacement equation, $\nabla \cdot (\gamma \nabla \xi) = 0$. A quadratic inverse-face-distance diffusivity ($\gamma = 1/\sqrt{d}$) referenced the trunk and the caudal fin enforces near-rigid motion close to the bodies which smoothly dissipates away from them (40). The dimensions of the grid are selected to mitigate the cell displacement to ensure that the moving mesh does not negatively influence the numerical interpolation between cells.

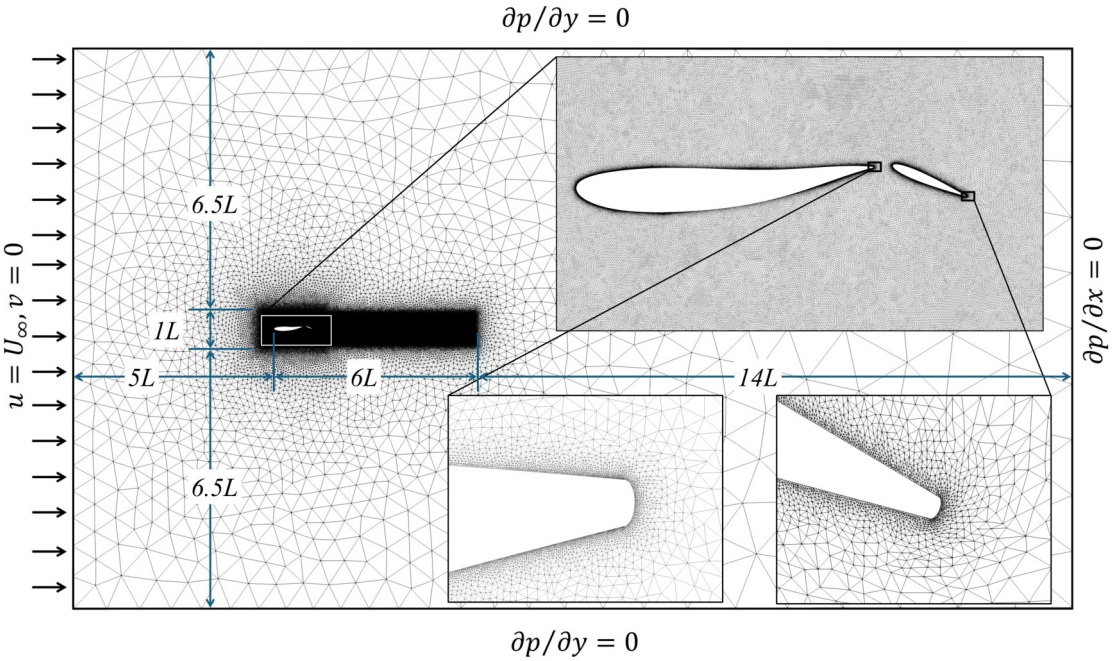

Figure 2.3: Flow domain and boundary conditions.

2.3 Verification and validation study

2.3.1 Two-Dimensional verification

We choose three grid resolutions to ensure the verification of our computational settings. For the grid-convergence and time step-independent studies, the Reynolds number is set as 500, $J^* = 0.125$, $f^* = 0.6$, and $\zeta = 1.0$. We select the final grid based on the reduction in relative error: Grid 1 with $307,489$ cells (Coarse Grid), Grid 2 with $483,623$ cells (Medium Grid), and Grid 3 with $651,687$ cells (Fine Grid). The body undergoes undulation, and the tail exhibits active heaving and passive pitching. The results of our simulations using the three grids are presented in Fig. 2.5a - 2.5f to compare the hydrodynamic force and moment coefficients of both the body and the tail as well as the pitching angle of the tail for the complete undulation cycle. Here C_L, C_D, and C_M

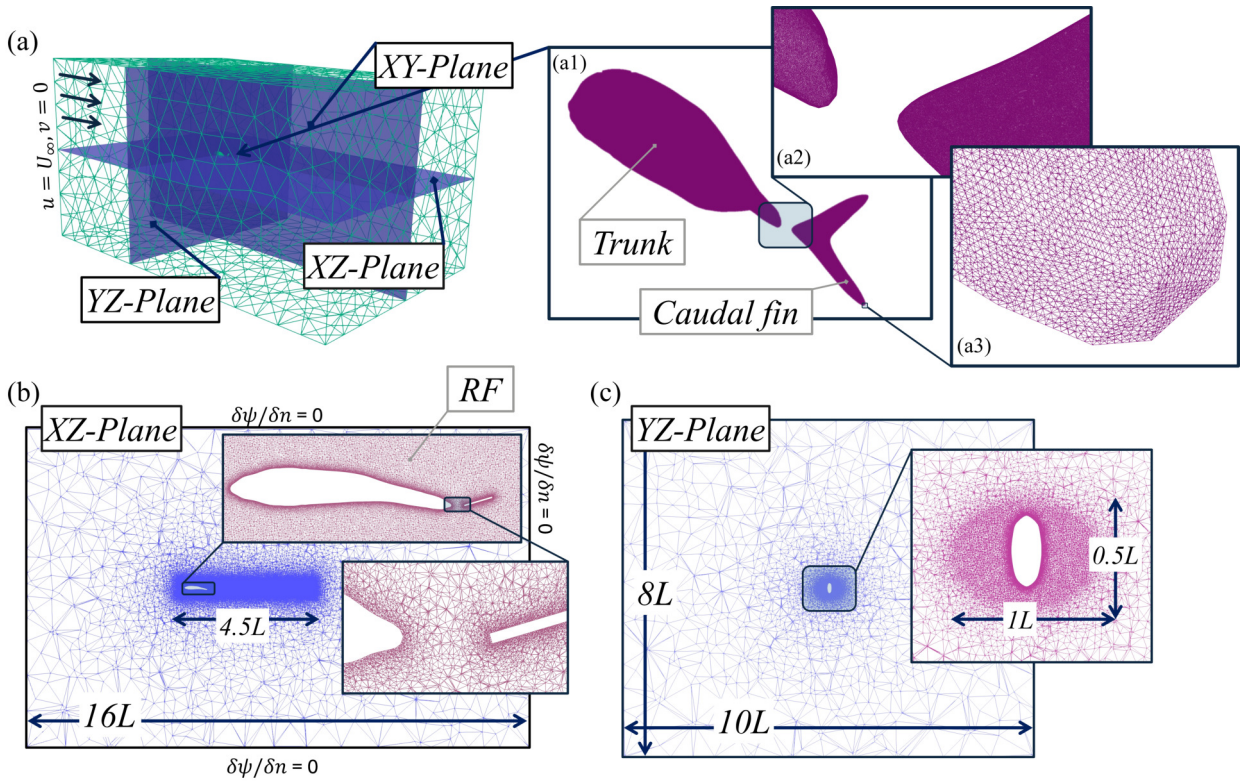

Figure 2.4: Flow domain and boundary conditions.

denote the lift coefficient, drag coefficient, and moment coefficient, respectively, normalized based on the Eqs. 2.11. Although no significant difference is observed in the computed values of C_L, C_D, and C_M for the body and tail, a clear improvement in capturing the pitching dynamics of the tail is found when the grid resolution is increased from the coarse to the medium grid. Based on these results, we select the medium grid for our next simulations.

$$C_L = \frac{2F_y}{\rho\, U_\infty^2\, A_{ref}}, C_D = \frac{2F_x}{\rho\, U_\infty^2\, A_{ref}}, C_M = \frac{2M}{\rho\, U_\infty^2\, A_{ref}\, c_t} \tag{2.11}$$

Next, We proceed with the time-step independence study, for which we choose three values of the time step size (Δt) so that the results stay unaffected by the selection of Δt. We choose 4000, 7500, and 10000 time steps per oscillation cycles for this study. Figure 2.6 shows the compar-

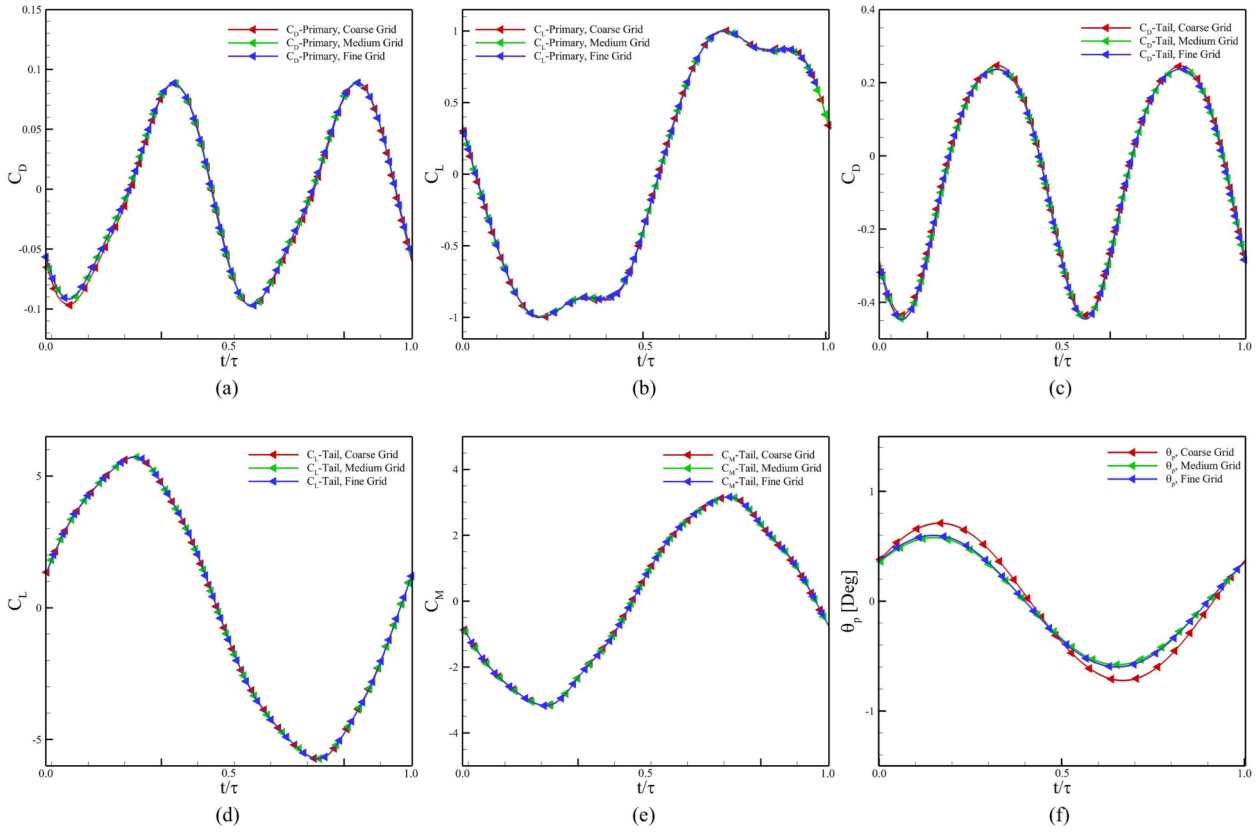

Figure 2.5: Results for convergence of Grid size.

ison of the hydrodynamic force and moment coefficients for the body and the tail for one complete undulation cycle. Based on the pitching-angle profiles, we choose to proceed with Δt according to 7500 time steps in one undulation cycle.

Our computational methodology and the strategy for the morphing mesh is validated by comparing the C_T, C_L with Gao et al. (1).Here, the Undulatory flexure over the main body c_b is defined with a Gaussian envelope, whereas the kinematic parameters used for the validation study are defined in Table 2.2. The force coefficients, C_T and C_L are employed here, where the comparison of the present results with those rfom Gao et al. (1) is presented in Fig. 2.7. Please note that $C_T = -C_D$. We find a very close agreement between both sets of data, that indicates the accuracy of our simulation methodology.

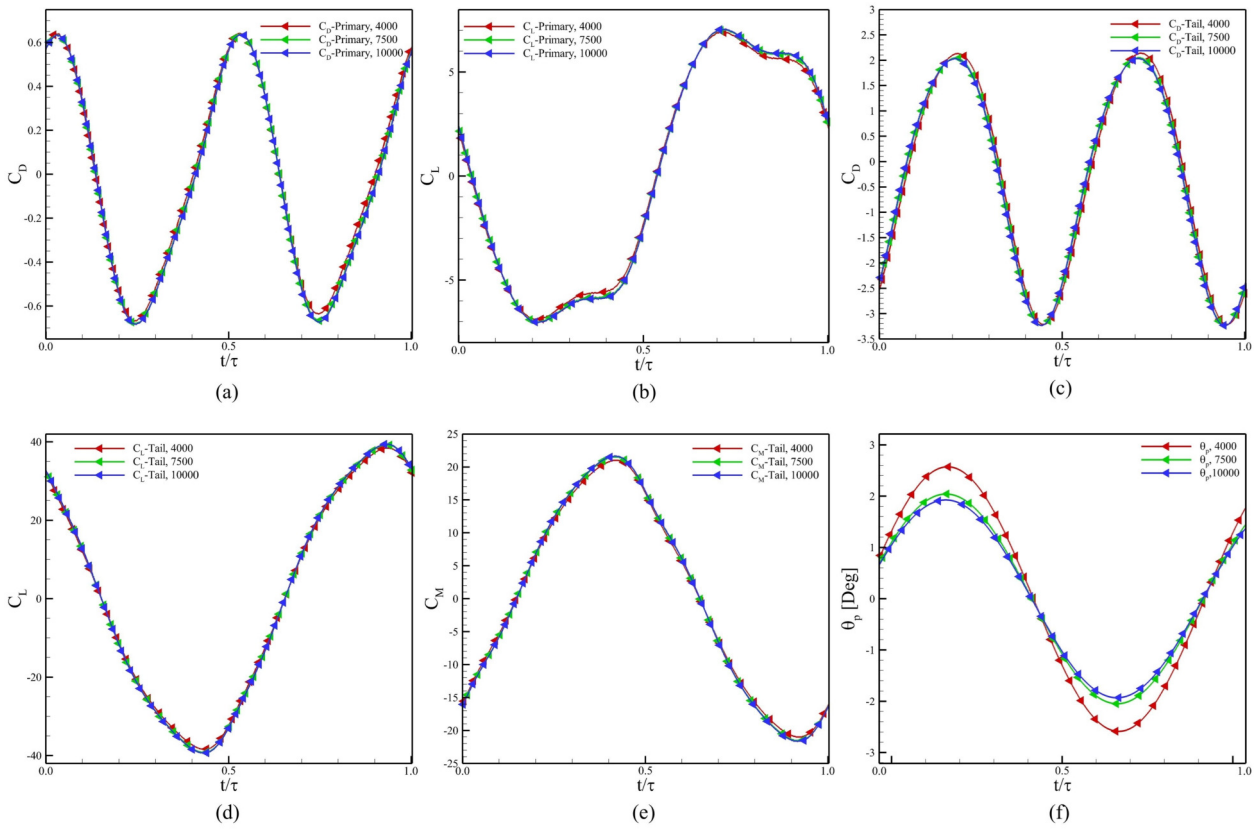

Figure 2.6: Results for convergence of Time step.

Table 2.2: Specifications of governing parameters for simulation methodology

Parameter	Symbol	Value
Reynolds number	Re	5000
Ratio between the heave amplitude and the length of the body	h/c_t	0.30
strouhal frequency	f^*	0.35
Phase between the heaving and pitching motion of the tail	ϕ_p	1.47
Undulating amplitude for the body	a_0	0.045

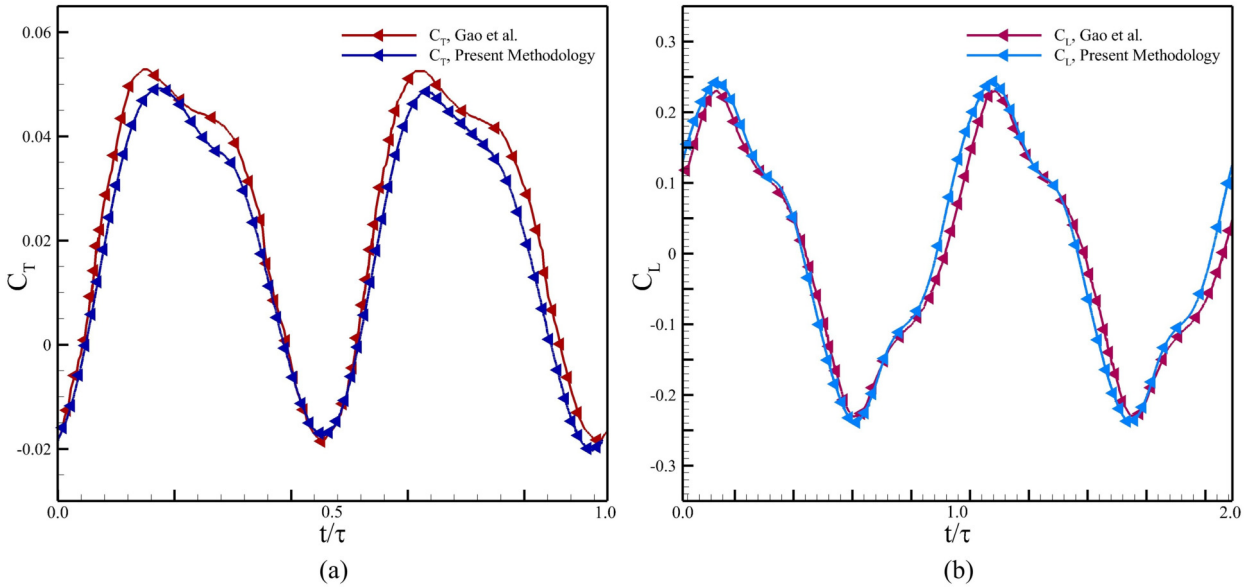

Figure 2.7: Comparison of our results (a) C_T, and (b) C_L with those of Gao et al (1).

2.3.2 Three-Dimensional verification

We choose three grid resolutions to ensure the verification of our computational settings. For the grid-convergence study, the Re = 3000, and $f^* = 0.6$ is choosen with an actively pitching caudal fin. We select the coarse grid from the three grids: Grid 1 with 14M cells (Coarse Grid), Grid 2 with 29M cells (Medium Grid), and Grid 3 with 56M cells (Fine Grid). The levels of refinement and comparison between the cell size near the boundaries are listed as shown in Table. 2.3. As seen in the Figs. 2.8a - c The dorsal view of the swimmer shows no significant difference in the coherent structures downstream in the wake of the swimmer between the coarse, medium, and fine grids. Furthermore, we can see the drag coefficient (C_D), and the lift coefficient (C_L) from Figs. 2.8d, and e, the relative error between the coarse, medium, and fine grid is significantly low which solidifies the reason for selecting the coarse grid. For this study, we choose the value of the time step size (Δt) based on 7500 time steps per oscillation cycle validated by Nayak et al. (41)

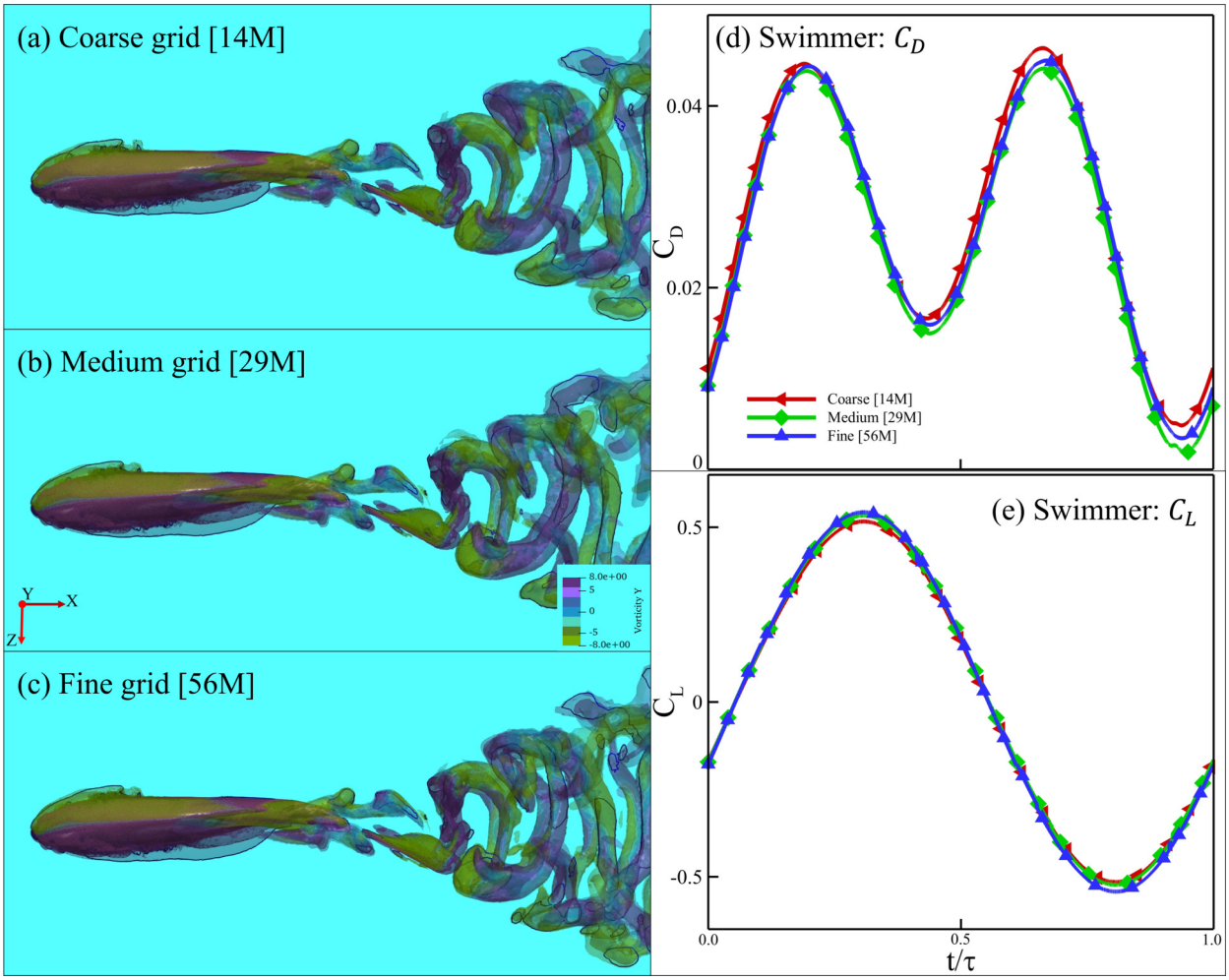

Figure 2.8: Results for convergence of Grid size.Pot with $Q = 40$ with the y-vorticity shows the iso-surface for (a) the coarse grid, (b) medium grid, and (c) fine grid. The Drag coefficient (C_D), and (d), and Lift coefficient (C_L) is plotted for all three grids for grid convergence analysis.

Our computational methodology and the strategy for the morphing mesh is validated by comparing the thrust coefficient C_T ($C_T = -C_D$). With three distinct cases corresponding to three values of wavelengths $\lambda = 0.925, 1.05$, and 1.25 as shown in Figs. 2.9a, b, and c, respectively with that of Khalid et al. (35). The plots show similar trend to reference case, the validation shows that the peak in the oscillation cycle occurs in the first half of the oscillation cycle for $\lambda = 0.925$ as shown in Fig. 2.9a, whereas for larger wavelength we observe that peak in C_T occurs in the second

Table 2.3: Mesh refinement details between coarse, medium, and fine grids. Refinement (I) denotes the comparison between Coarse and Medium, while Refinement (II) denotes the comparison between Medium and Fine.

	Coarse	**Medium**	**Refinement (I)**	**Medium**	**Fine**	**Refinement (II)**
Cells	13,764,344	28,665,094	**52%**	28,665,094	55,629,584	**48%**
Body	0.0015	0.0008	**47%**	0.0008	0.00055	**31%**
Tail	0.0010	0.0006	**40%**	0.0006	0.00035	**42%**
RF	0.0085	0.0070	**18%**	0.0070	0.0065	**7%**

half of the oscillation cycle as shown in Figs. 2.9b and c.

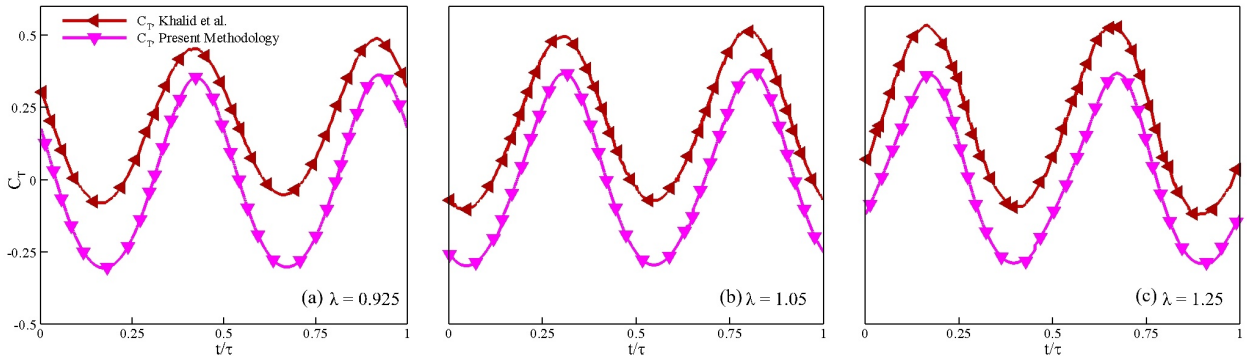

Figure 2.9: Flow domain and boundary conditions.

Chapter 3

2D Investigations of Caudal Fins of Carangiform Swimmers

The governing parameters are selected to ensure effective simulation performance. The wavelength is fixed at $\lambda = 1.0$. The Strouhal frequency f^* and damping ratio ζ are varied in increments of 0.1 and 0.2, respectively, within the ranges shown in Table 3.1. The non-dimensional inertia J^* is adjusted in steps of 0.125. The torsional spring stiffness for passive pitching depends on J^*, n, c_t, a, and f^*, as expressed in Equation 2.5. Relevant kinematic parameters are summarized in Table 3.1.

3.1 Quantitative analysis on actively pitching tail

A common modeling approach approximates the body of a carangiform swimmer as a single airfoil (13; 34–36; 42), as illustrated in Fig. 3.1a. In this study, we instead adopt a biomimetic two-foil configuration, representing the body and tail as separate foils, as shown in Fig. 3.1b. To ensure a

Table 3.1: Specifications of governing parameters for 2D analysis

Parameter	Symbol	Value
Undulatory gait	—	Carangiform
Strouhal frequency	f^*	0.2-0.6
Damping ratio	ζ	0-1.0
Dimensionless inertia	J^*	0.125, 0.250, 0.375
Reynolds number	Re	500, 5000
Primary-foil chord length	c_b	$0.75\,L$
Secondary-foil chord length	c_t	$0.20\,L$

consistent tail trajectory across all cases, the prescribed flapping motion is constrained so that the centerlines of the body and tail remain continuous. The amplitude trailing-edge amplitude of the tail is matched to the undulatory envelope of a carangiform swimmer at the posterior section of the body, with a maximum lateral amplitude of $A(1.0) = 0.1L$. Since the geometry and flow conditions are identical for both the actively and passively pitching tails, a direct comparison can be made to evaluate how hydrodynamic performance changes when the kinematics of the tail are switched from active to passive. In this framework, the heaving displacement of the tail is prescribed to follow the undulation of the body at its peduncle, while the kinematics of the tail with active pitching is defined by Eq. 3.1.

$$\theta_p(t) = f\,(t)\,\sin^{-1}\left\{\frac{1}{c_t}\left[A(1.0)\,\cos\left(2\pi\left(\tfrac{1.0}{\lambda} - ft\right)\right) - A(0.8)\,\cos\left(2\pi\left(\tfrac{0.8}{\lambda} - ft\right)\right)\right]\right\}. \tag{3.1}$$

where θ_p denotes the angle.

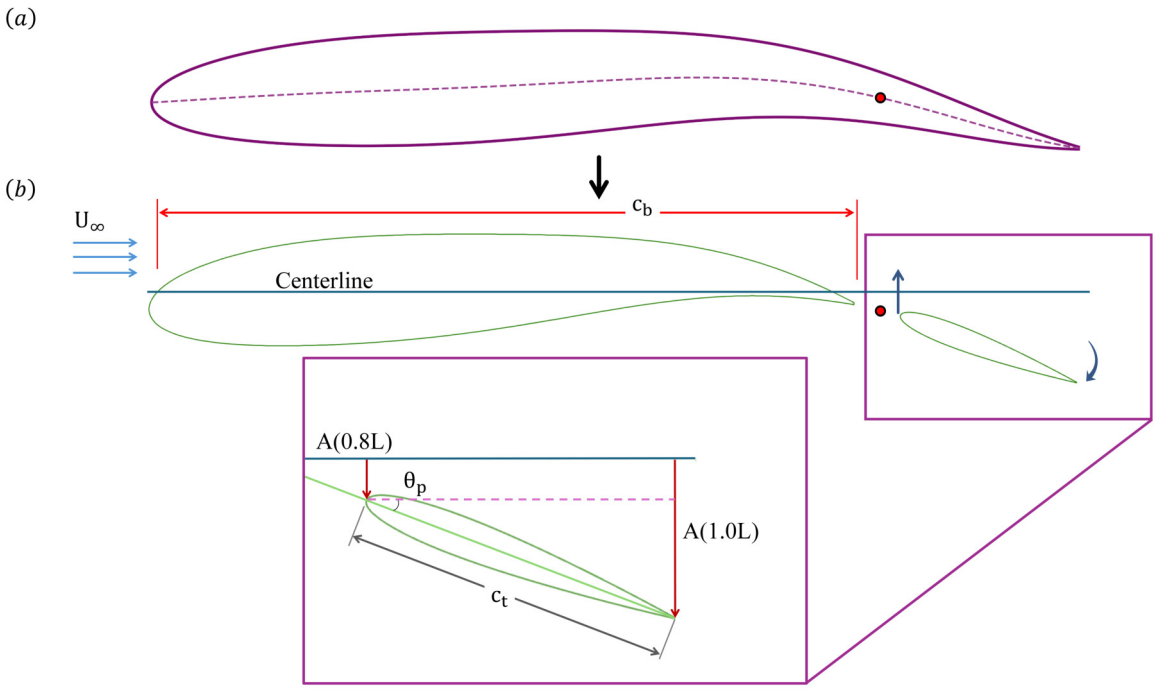

Figure 3.1: Model of the actively pitching tail mimicking a swimmer with continuous undulatory flexure.

For the actively pitching-tail configuration, a total of ten simulations are conducted at Re = 500 and Re = 5000, covering five Strouhal frequencies in the range $f^* = 0.2$–0.6. The maximum pitching angle of the tail, $(\theta_p)_{\max} = 30°$, is defined as the angle between the leading edge and the centerline at its peak within an oscillation cycle (see Fig. 3.1). The resulting motion produces a phase difference (Ψ) of 112° between the heaving and pitching of the tail. The performance of the tail is evaluated in terms of the ratio between the output power and input power, expressed as a power ratio (η) defined by Eq. 3.2. The power coefficients $C_{P,\text{heave}}$, $C_{P,\text{pitch}}$, and $C_{P,\text{thrust}}$ are obtained from Eqs. (3.3)–(3.5), following the methodology of Picard *et al.* (43) and Wu *et al.* (44). For the actively pitching cases, $C_{P,\text{thrust}} = C_{P,\text{out}}$, and the $C_{P,\text{heave}}+C_{P,\text{pitch}}= C_{P,\text{in}}$. And for the passively pitching tail, the $C_{P,\text{thrust}} + C_{P,\text{pitch}}= C_{P,\text{out}}$, and the $C_{P,\text{heave}}= C_{P,\text{in}}$

$$\eta = \frac{C_{P,\text{out}}}{C_{P,\text{in}}} \tag{3.2}$$

$$C_{P,\text{heave}}(t) = C_L(t) \cdot \frac{\dot{h}_{\text{heave}}(t)}{U_\infty} \tag{3.3}$$

$$C_{P,\text{pitch}}(t) = C_{M,\text{pitch}}(t) \cdot \frac{\dot{\theta}_{\text{pitch}}(t) \cdot c_t}{U_\infty} \tag{3.4}$$

$$C_{P,\text{thrust}}(t) = -C_D(t) \tag{3.5}$$

Table 3.2: Time-averaged power coefficients and power ratio (η) of the actively pitching tail at Re = 500 and Re = 5000.

	Re = 500					Re = 5000				
f^*	$\overline{C_{P\text{heave}}}$	$\overline{C_{P\text{pitch}}}$	$\overline{C_{P\text{out}}}$	$\overline{C_{P\text{in}}}$	η [%]	$\overline{C_{P\text{heave}}}$	$\overline{C_{P\text{pitch}}}$	$\overline{C_{P\text{out}}}$	$\overline{C_{P\text{in}}}$	η [%]
0.20	0.434	0.168	0.003	0.602	0.4	0.226	0.451	0.145	0.677	21.4
0.30	1.530	0.957	0.260	2.487	10.4	1.099	1.621	0.611	2.720	22.5
0.40	3.723	2.798	0.750	6.521	11.5	3.016	4.121	1.399	7.138	19.6
0.50	7.389	6.099	1.484	13.489	11.0	6.462	8.338	2.514	14.799	17.0
0.60	12.903	11.231	2.465	24.134	10.2	11.807	14.767	3.959	26.574	14.9

Here, $\dot{h}_{\text{heave}}$ and $\dot{\theta}_{\text{pitch}}$ denote the heaving and pitching velocities of the tail, respectively. The normalized mean power consumed by the tail to heave ($\overline{C}_{P,\text{heave}}$) and pitch ($\overline{C}_{P,\text{pitch}}$), alongside the output power ($\overline{C}_{P,\text{out}}$) for the actively pitching tail, are computed at Re = 500 and Re = 5000.

As summarized in Table 3.2, the power-ratio η increases significantly between Re =500 to 5000, indicating more favorable energy transfer at Reynolds number 5000. A consistent drop in η is observed at $f^* = 0.6$ for both Reynolds numbers, while a low value of power ratio ($\eta = 0.4\%$) occurs at $Re = 500$ and $f^* = 0.2$, corresponding to negligible thrust output ($\overline{C}_T = -\overline{C}_D \approx 0$) as per the relationship from Eq. 3.2.

Table 3.3: Time-averaged drag coefficients of the actively pitching tail at Re = 500 and Re = 5000.

	Re = 500	Re = 5000
f^*	$\overline{C}_{D,\,tail}$	$\overline{C}_{D,\,tail}$
0.20	−0.003	−0.145
0.30	−0.260	−0.611
0.40	−0.750	−1.399
0.50	−1.484	−2.514
0.60	−2.465	−3.959

Table 3.3 presents the variation of the mean drag coefficient with an increasing f^* for the tail of the swimmer. The results show a clear transition from near-zero thrust at low f^* to increasingly negative values as the frequency rises, indicating a corresponding increase in thrust. Furthermore, at Re = 5000, the negative mean drag coefficient (positive thrust) is consistently larger in magnitude than at Re=500, showing larger thrust generation at the higher Reynolds number.

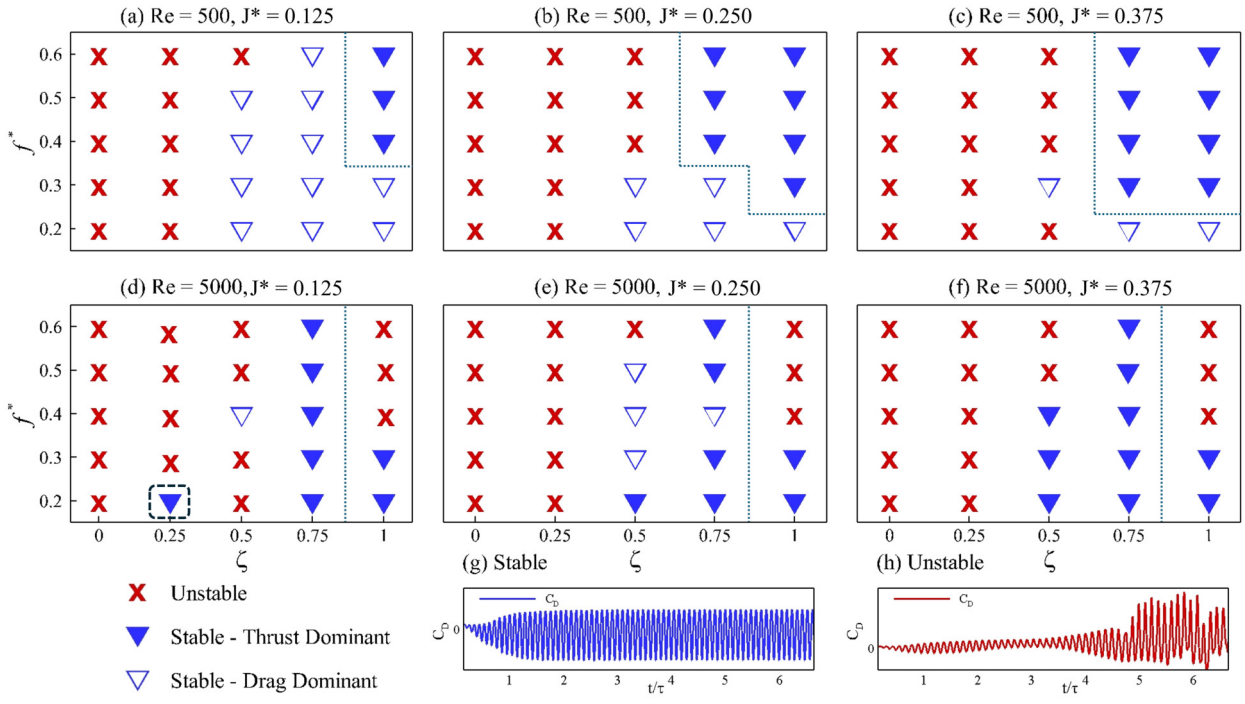

Figure 3.2: Stability map (a)-(f) insets illustrate C_D for a typical stable (g) and unstable (h) cases.

3.2 Quantitative analysis on passively pitching tail

Before discussing the dynamics of the swimmer with a passively pitching tail, we note that a total of 150 numerical simulations are performed. The responses are categorized into three modes: stable drag-dominated, stable thrust-dominated, and unstable. This classification is summarized in Fig. 3.2, which we refer to as the stability maps, constructed for different sets of kinematic and flow parameters. The classification is based on 40 oscillation cycles. A case is considered stable if the flow reaches a periodic steady state within this window; otherwise, it is classified as unstable. Stability is determined using the drag coefficient (C_D): if a case fails to reach a steady state (Fig. 3.2h), the case is labeled as unstable, whereas cases that converge to steady periodic behavior (Fig. 3.2g) are labeled stable. Although steady state is typically achieved within 5–8

cycles, 40 cycles are simulated to ensure complete decay of transient effects and convergence to steady state. Stable cases are further categorized using the mean drag coefficient ($\overline{C_D}$). If $\overline{C_D} > 0$, the case is classified as stable drag-dominated; if $\overline{C_D} < 0$, it is classified as stable thrust-dominated.

Across the stability maps, three clear patterns emerge. First, every undamped configuration ($\zeta = 0$) diverges, confirming the requirement of minimal damping needed for a bounded motion of the passively pitching tail. Introducing a light damping ($\zeta = 0.25$) causes the tail to drift in and out of the thrust-producing region, highlighted by the dashed rectangle in Fig. 3.2(d), illustrating the decisive influence of fluid–structure coupling on the net force. At Re = 500, stability improves with a higher inertia, with the tail exhibiting a stable dynamic response at Re = 500, and the majority of the cases at Re = 5000. In these cases, the response becomes thrust-dominated, as the f^* increases from left to right. The consistent trends that we observe at Re = 500 do not stay true when the Reynolds number is changed to 5000. At Re = 5000, the trend of stable and unstable cases stays consistent at $\zeta = 0.75$ and $\zeta = 1$, but the inconsistency based on the f^* is prominent at $\zeta = 0.25$ and $\zeta = 0.50$

We now turn to the passively pitching tail and analyze its drag coefficient for all stable cases. It allows us to assess how the transition from active to passive pitching influences the performance of the swimmer, based on the mean drag coefficient presented in Fig. 3.3. Figures 3.3a and 3.3b show the mean drag coefficient ($\overline{C_D}$) of the tail at Re = 500 and Re = 5000, respectively. From Fig. 3.3a, the first observation is that the configuration with $\zeta = 0.50$ and $J^* = 0.125$ exhibits an increasing $\overline{C_D}$ (i.e., decreasing thrust) as the f^* increases to 0.5. Beyond this point, at $f^* = 0.6$, the case becomes unstable. Secondly, for the same value of inertia ($J^* = 0.125$) but with a higher $\zeta = 0.75$, the trend remains nearly constant across the range of Strouhal frequencies considered here. When this trend is compared to that of at $\zeta = 0.5$ a large shift, increasing the damping ratio shows a

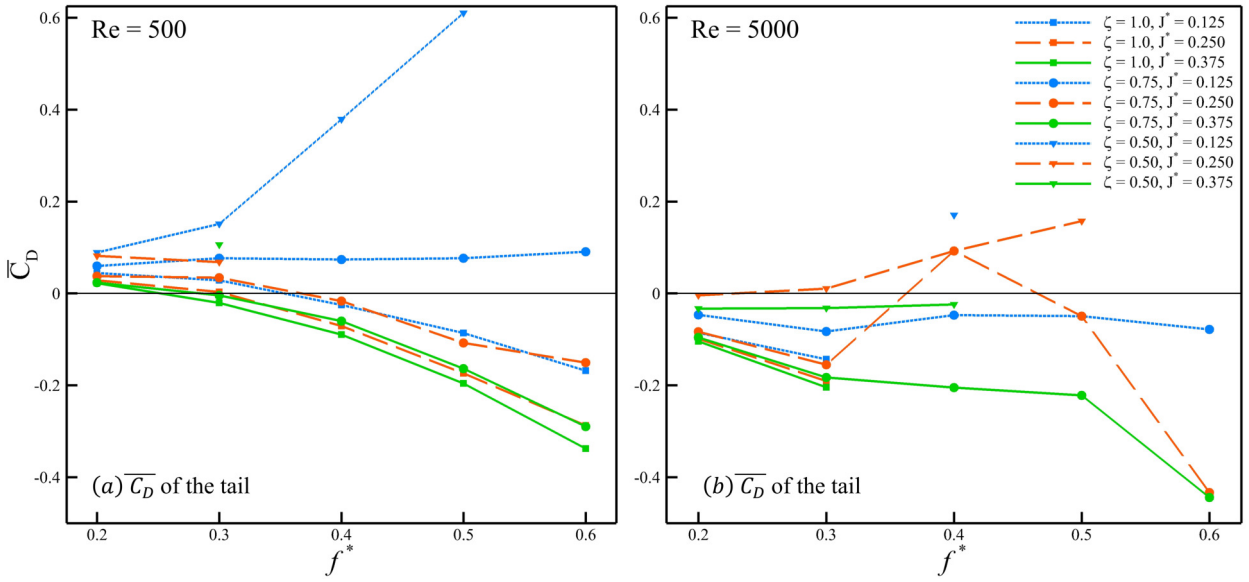

Figure 3.3: Mean drag coefficient of the passively pitching tail at (a) Re = 500, and (b) 5000.

reduction of $\overline{C_D}$. Further increasing the damping ratio ($\zeta = 1.0$), the trend shows a behavior similar to that of the actively pitching tail where the thrust increases as the Strouhal frequency is increased. Finally, examining the stable cases with a passively pitching tail, at $\zeta = 0.50$ for a range of inertia values ($J^* = 0.125$–0.375), neither of the cases fully transition towards producing positive thrust ($\overline{C_D} < 0$). However, all of the cases display a reduction in drag with an increase in inertia, and this trend of drag reduction with a higher inertia is consistently observed for all damping ratios chosen for this work.

At Re = 5000 shown in Fig. 3.3b, the number of stable cases decreases, making it more difficult to identify clear trends and assess the effect of Strouhal frequency on the mean drag coefficient. Compared to the cases at Re = 500, the configurations that remain stable at Re = 5000 generally show better performance in terms of mean thrust. However, despite the improvement when the Reynolds number increases, the inconsistencies in the trends make it difficult to draw firm conclusions about the role of the Strouhal frequency. Based on the trends observed in Figs. 3.3a and 3.3b,

the behavior of the swimmer about its peduncle can be interpreted by categorizing the tail into three types according to its inertia $J^* = 0.125 - 0.375$. While the inertia defines the characteristic response of the tail itself, the damping ratio characterizes the nature of its joint to the body. A lower damping ratio corresponds to a more loosely joined and flexible body and tail connection, whereas a higher damping ratio indicates a stiffer and less flexible joint.

(a) $f^* = 0.20$

J^*	ζ	Re = 500		Re = 5000	
		$\overline{C}_D$	$\theta_{p,\max}$	$\overline{C}_D$	$\theta_{p,\max}$
0.125	0.50	0.09	7.18	N/A	N/A
	0.75	0.06	4.59	−0.05	4.84
	1.00	0.05	3.09	−0.09	3.40
0.250	0.50	0.09	5.69	−0.01	6.84
	0.75	0.04	3.00	−0.08	3.07
	1.00	0.03	1.93	−0.10	1.94
0.375	0.50	N/A	N/A	−0.03	5.68
	0.75	0.02	1.34	−0.10	2.21
	1.00	0.02	1.34	−0.10	1.34

(b) $f^* = 0.30$

J^*	ζ	Re = 500		Re = 5000	
		$\overline{C}_D$	$\theta_{p,\max}$	$\overline{C}_D$	$\theta_{p,\max}$
0.125	0.50	0.15	7.26	N/A	N/A
	0.75	0.08	4.62	−0.08	4.53
	1.00	0.03	3.32	−0.14	3.18
0.250	0.50	0.07	4.68	0.01	6.41
	0.75	0.04	3.01	−0.16	2.88
	1.00	0.01	1.83	−0.19	1.84
0.375	0.50	0.11	5.24	−0.03	5.16
	0.75	−0.01	2.20	−0.18	2.09
	1.00	−0.02	1.35	−0.20	1.28

(c) $f^* = 0.40$

J^*	ζ	Re = 500		Re = 5000	
		$\overline{C}_D$	$\theta_{p,\max}$	$\overline{C}_D$	$\theta_{p,\max}$
0.125	0.50	0.38	8.16	0.17	6.30
	0.75	0.07	5.12	−0.05	4.30
	1.00	−0.03	3.54	N/A	N/A
0.250	0.50	N/A	N/A	0.09	5.89
	0.75	−0.02	3.19	0.09	5.89
	1.00	−0.07	1.98	N/A	N/A
0.375	0.50	N/A	N/A	−0.02	4.99
	0.75	−0.06	2.21	−0.21	2.12
	1.00	−0.09	1.35	N/A	N/A

(d) $f^* = 0.50$

J^*	ζ	Re = 500		Re = 5000	
		$\overline{C}_D$	$\theta_{p,\max}$	$\overline{C}_D$	$\theta_{p,\max}$
0.125	0.50	0.61	8.19	N/A	N/A
	0.75	0.08	5.12	−0.05	2.96
	1.00	−0.09	3.54	N/A	N/A
0.250	0.50	N/A	N/A	0.16	6.17
	0.75	−0.11	3.18	−0.05	2.39
	1.00	−0.18	1.97	N/A	N/A
0.375	0.50	N/A	N/A	N/A	N/A
	0.75	−0.17	2.28	N/A	N/A
	1.00	−0.20	1.37	N/A	N/A

(e) $f^* = 0.60$

J^*	ζ	Re = 500		Re = 5000	
		$\overline{C}_D$	$\theta_{p,\max}$	$\overline{C}_D$	$\theta_{p,\max}$
0.125	0.50	N/A	N/A	N/A	N/A
	0.75	0.09	5.23	−0.08	4.12
	1.00	−0.17	3.63	N/A	N/A
0.250	0.50	N/A	N/A	N/A	N/A
	0.75	−0.15	3.24	−0.44	2.98
	1.00	−0.29	2.02	N/A	N/A
0.375	0.50	N/A	N/A	N/A	N/A
	0.75	−0.30	2.31	−0.45	2.13
	1.00	−0.34	1.39	N/A	N/A

Table 3.4: Data on stable cases presenting the mean drag coefficient ($\overline{C_D}$) and maximum pitching angle ($\theta_{p,\max}$) of the passively pitching tail across Strouhal frequencies (f^*), damping ratios (ζ), and inertia ratios (J^*) at Reynolds numbers Re = 500 and Re = 5000.

The nature of the joint between the body and the tail of the swimmer influences its thrust performance, as discussed earlier. From the previous analysis, a stiffer joint between the body and the tail corresponds to higher thrust or a more thrust-dominant behavior, whereas a more flexible or looser joint leads to a drag-dominant response. Table 3.4 presents the maximum pitching angle ($\theta_{p,\max}$) alongside the mean drag coefficient ($\overline{C_D}$) of the tail at Re = 500 and Re = 5000 for all stable cases. The results are grouped in Table 3.4a–3.4e according to the Strouhal frequency ($f^* = 0.2$–0.6). Here, *N/A* indicates values that could not be evaluated due to the unstable nature of the configuration, as identified in the stability maps shown in Figs. 3.2a–3.2f.

Analyzing the effect of Strouhal frequency, for a given configuration of J^* and ζ, an increase in f^* leads to a larger maximum pitching angle ($\theta_{p,\max}$). It is accompanied by a clear trend of decreasing mean drag coefficient ($\overline{C_D}$) or equivalently increasing thrust ($-\overline{C_D}$), a behavior consistent at both Re = 500 and Re = 5000. However, when f^* and ζ are held constant to isolate the effect of J^*, $\theta_{p,\max}$ decreases alongside decreasing $\overline{C_D}$. A similar trend is observed when f^* and J^* are fixed and ζ is varied. These observations suggest that a larger pitching amplitude is beneficial only when achieved by increasing the Strouhal frequency. In contrast, when the larger amplitude results from reduced inertia or damping ratio at a fixed Strouhal frequency, it adversely affects thrust generation.

The swimmer with an actively pitching tail generates higher thrust than its passive counterparts. In these cases, a pitching amplitude of 30° is required to ensure that the trailing edge of the tail spans the peak-to-peak amplitude of the carangiform swimmer ($A(L) = 0.1L$). The heaving amplitude of the tail, defined as the displacement of the peduncle, is $A(0.78) = 0.0525L$, which is relatively smaller than the pitching amplitude of an actively pitching tail. When such a large angular amplitude (pitching) is combined with a small linear amplitude (heaving), the power

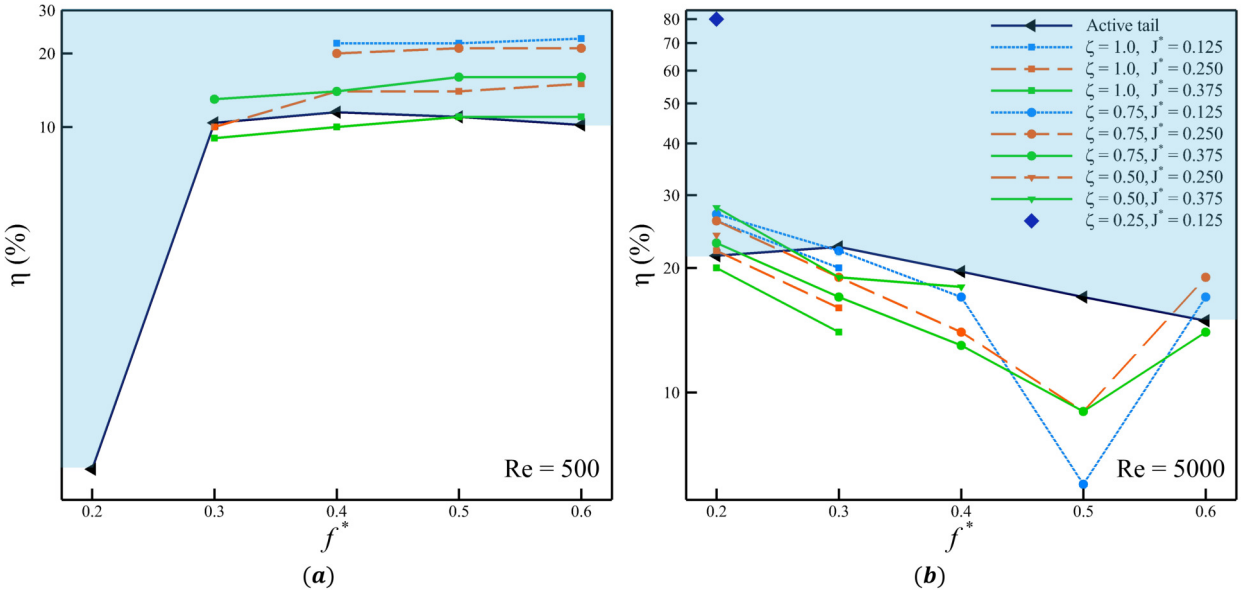

Figure 3.4: Power ratio at (a) Re = 500, and (b) 5000.

expenditure increases significantly, particularly at higher Strouhal frequencies. The larger peak-to-peak amplitude corresponds to greater thrust production. In contrast, for the passively pitching tail, the maximum observed pitching angle does not exceed $\theta_{p,\max} = 8.2°$. This reduced pitching angle explains the lower thrust coefficients observed. However, it also results in a lower-power swimming mode, as the pitching of the tail requires less input power. These two contrasting behaviors are captured quantitatively by the power ratio (η), shown in Fig. 3.4.

Figures 3.4a and 3.4b show the η as a function of f^* for Re = 500 and Re = 5000, respectively. The power ratio is plotted on the logarithmic scale to capture the full range of values and trends. The solid black line represents the power ratio for the actively pitching tail, which serves as a reference for comparison with the cases with a passively pitching tail. The region above this line highlighted in blue represents the configurations where the tail with passive pitching outperforms the active counterpart. At Re = 500, a significant number of cases with a passively pitching tail achieve higher η than those with the active tail. As f^* increases, the power ratio of the cases with

a passive tail shows a modest upward trend, whereas the cases with the active tail only peaks at $f^* = 0.4$ and then decreases subsequently. Indicating that at lower Reynolds numbers, the passive tail often provides a performance advantage based on the η.

In contrast, at Re = 5000, most of the cases with a passively pitching tail exhibit lower power ratios than their active counterparts. Only a limited number of configurations outperform the active case, and these are again concentrated near $f^* = 0.2$. Thus, the overall trend shifts with Reynolds number: passively pitching tails show superior performance at Re = 500, while actively pitching tails dominate at Re = 5000. When the passively pitching tail configurations are compared in terms of its thrust production and power ratio as performance metrics, a consistent trade-off emerges. Configurations that generate larger mean thrust tend to exhibit lower power ratios, whereas those with lower mean thrust generally achieve higher power ratios. An intermittent case at $Re = 5000$, with $\zeta = 0.25$ and $J^* = 0.125$, shows a unique transition from thrust-dominant to drag-dominant behaviour and back to thrust-dominant behaviour. This case reaches a maximum pitching angle of 25° and is the only configuration among the 150 simulations to exhibit such dynamics. Given its rarity, This case is not examined further in the present study, primarily because no conclusive correlation or influence of any controlling parameter can be established.

3.3 Comparative Vortex Dynamics of Active and Passive Pitching Tails

From the quantitative analysis of the results, we observe a consistent trend for both the actively and passively pitching tails: as the Strouhal frequency increases, the thrust coefficient increases. To

further investigate this phenomenon, we examine the vortex street in the wakes of the swimmers at Re = 500, and 5000. To keep the discussion centered on the role of Strouhal frequency, we consider all cases of the actively pitching tail for increasing f^*. For the passively pitching tail, we focus on configurations with fixed parameters $\zeta = 1.0$ and $J^* = 0.375$, varying only the Strouhal frequency. Both stable and unstable configurations with a passively pitching tails are included to provide additional insight into the origin of the instabilities observed at a higher f^* seen earlier in the stability maps (Fig. 3.2).

We first examine the vortex dynamics of the swimmers at Re = 500, as shown in Fig. 3.5. The first column (Figs. 3.5a–3.5e) presents the contours of vorticity for cases with an actively pitching tail, whereas the second column (Figs. 3.5f–3.5j) corresponds to the cases with a passively pitching tail. For each case, we report report the $\overline{C_T}$, to quantify the propulsive performance associated with the observed wake structures. In Fig. 3.5, $1S$ denotes a single vortex shed into the wake during a half oscillation cycle.

From Figs. 3.5a and 3.5f, we observe that at $f^* = 0.2$, the vortex street in the wake of both swimmers is faint. Nevertheless, even from this weak signatures, it is clear that both wakes form a classical von Kármán vortex street, typically associated with drag-dominated flows. For the actively pitching tail, although the mean thrust coefficient $\overline{C_T}$ is positive, its value is too small to generate an effective thrust. As the f^* increases to 0.3 and 0.4 (Figs. 3.5b, 3.5g and 3.5c, 3.5h), the wake transitions to a reverse von Kármán vortex street in all cases. This transition coincides with increasing values of $\overline{C_T}$. With higher f^*, the strength of the coherent structures also intensifies. For the actively pitching tail at $f^* = 0.5$ and $f^* = 0.6$, the wake remains reverse von Kármán, with the vortices becoming progressively stronger and persisting further downstream (Figs. 3.5d–3.5e). It is consistent with the steady increase in $\overline{C_T}$ observed at higher Strouhal frequencies.

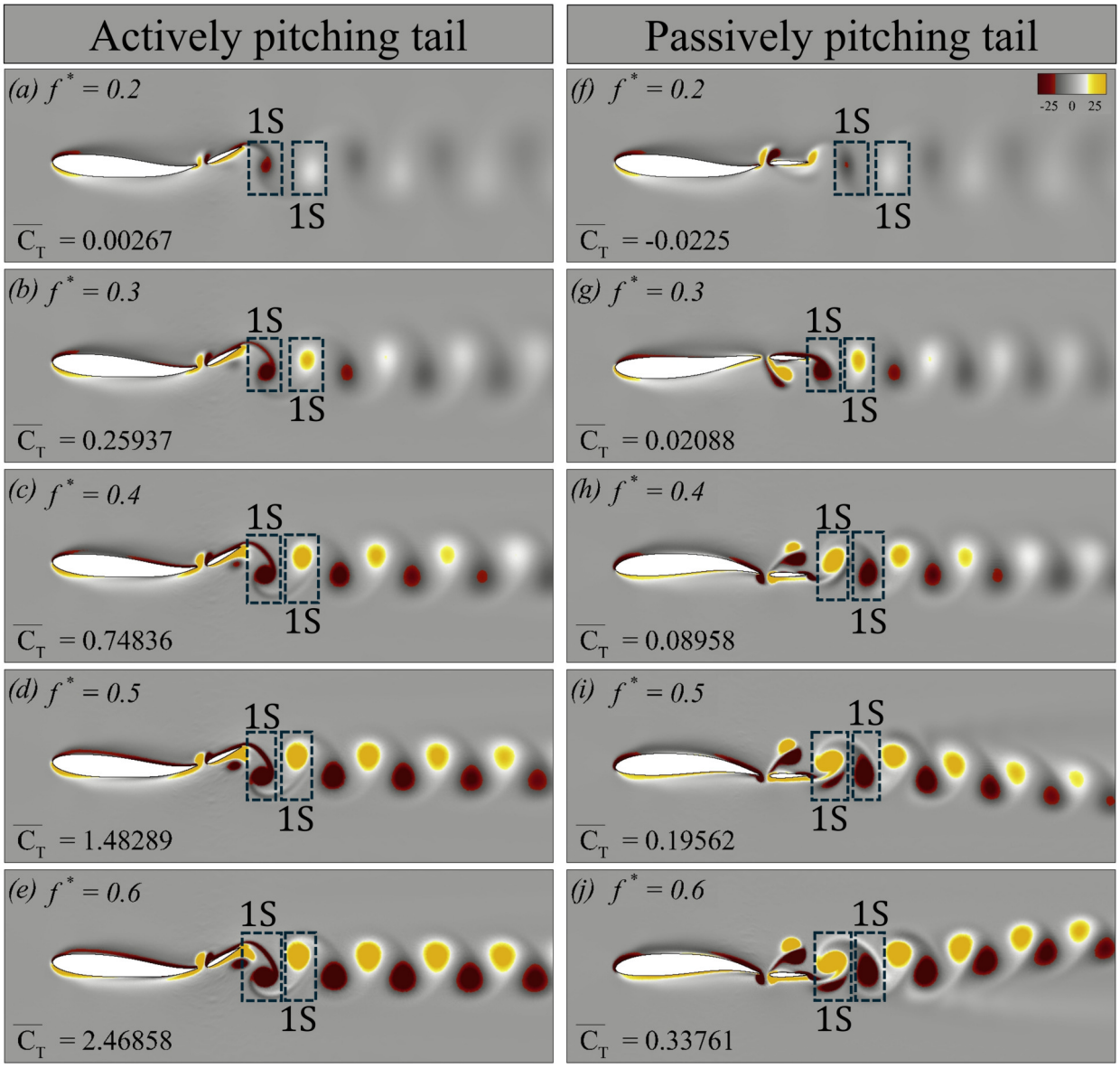

Figure 3.5: Vorticity contours corresponding to the swimmer with (a-e) an actively pitching tail, and (f-j) a passively pitching tail respectively at Re = 500.

In contrast, at $f^* = 0.5$ and $f^* = 0.6$, the passively pitching tail produces asymmetric wakes (Figs. 3.5i–3.5j). These asymmetric reverse von Kármán vortex streets are generally associated with stronger thrust-producing wakes. Godoy-Diana et al. (45) highlighted that such symmetry breaking occurred at high Strouhal frequencies. This asymmetry implies that the net force gener-

ated by the flapping tail is no longer aligned with the mid-plane of the swimmer.

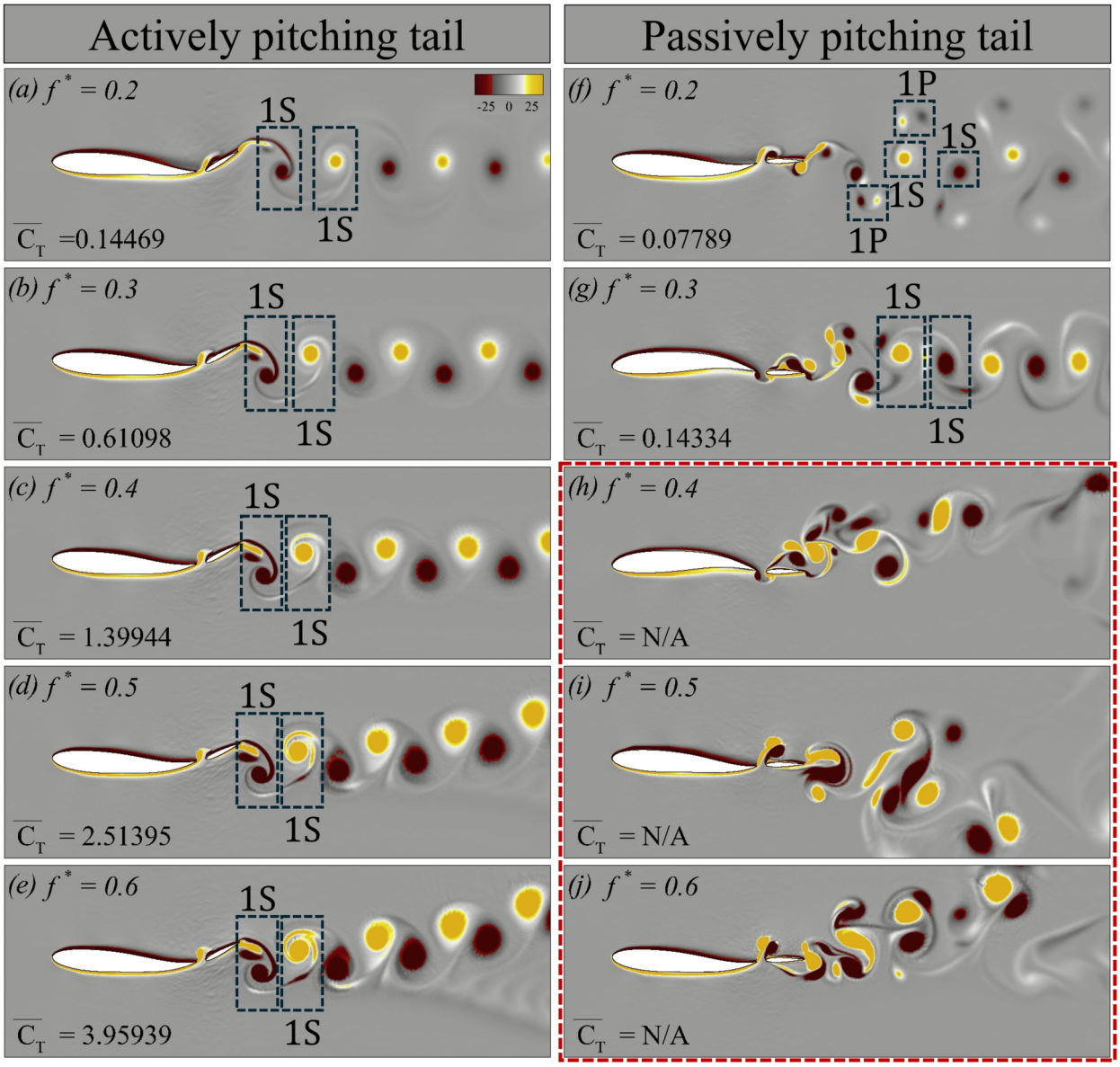

Figure 3.6: Vorticity contours corresponding to the swimmer with (a-e) an actively pitching tail, and (f-j) a passively pitching tail respectively at Re = 5000.

Similarly, we now examine the vortex dynamics of both swimmers at Re = 5000, as shown in Fig. 3.6. The overall layout of this figure is identical to that of Fig. 3.5. For the case with a passively pitching tail at $f^* = 0.4$–0.6, the results exhibit instabilities, as highlighted by the red

periphery in Figs. 3.6h–3.6j. In Fig. 3.6, $1P$ corresponds to a single vortex pair shed during a half oscillation cycle (one clockwise rotating vortex paired with a counter-clockwise rotating vortex).

Figures 3.6a and 3.6f show the wake topology of the actively and passively pitching tail configurations, respectively, at $f^* = 0.2$. For the case with an active tail, the wake resembles that observed at Re = 500, whereas the passive tail exhibits a $2S$–$2P$ shedding pattern. As the f^* increases to 0.3, the actively pitching tail maintains the same topology, while the passive tail develops a reverse von Kármán vortex street characterized by a $2S$ wake pattern. Although the wake corresponds to a reverse von Kármán street, minor instabilities begin to appear, as shown in Fig. 3.6g. For the actively pitching tail, an increasing Strouhal frequency continues to increase thrust, consistent with the trend observed at Re = 500. However, from $f^* = 0.4$–0.6, the wake becomes increasingly asymmetric, with the asymmetry becoming more pronounced at ma higher f^* (Figs. 3.6c–3.6e). On the other hand, for the passive tail, the red-outlined region (Figs. 3.6h–3.6j) highlights the growing instabilities in the wake as the Strouhal frequency increases.

From the earlier analysis of the power ratio at $f^* = 0.6$ and Re = 500, the passively pitching tail ($J^* = 0.125$, $\zeta = 1.0$) produce more than twice the power ratio of than an actively pitching tail at the same f^*. To better understand the effect of the flow on the tail, we examine the vortex dynamics of both configurations, shown side by side in Figs. 3.7. Figures 3.7(a) and 3.7(b) present the drag (C_D), lift (C_L), and moment (C_M) coefficients over one oscillation cycle for the cases with an actively pitching tail and a passively pitching tail, respectively. The corresponding z-vorticity fields are displayed in Figs. 3.7(c) and 3.7(d) at four time instants, capturing the motion as the body undulates from its uppermost position, descending to the lowest point, and ascending back to complete the full cycle. In both cases, the undulation of the body and the heaving of the tail remain in phase.

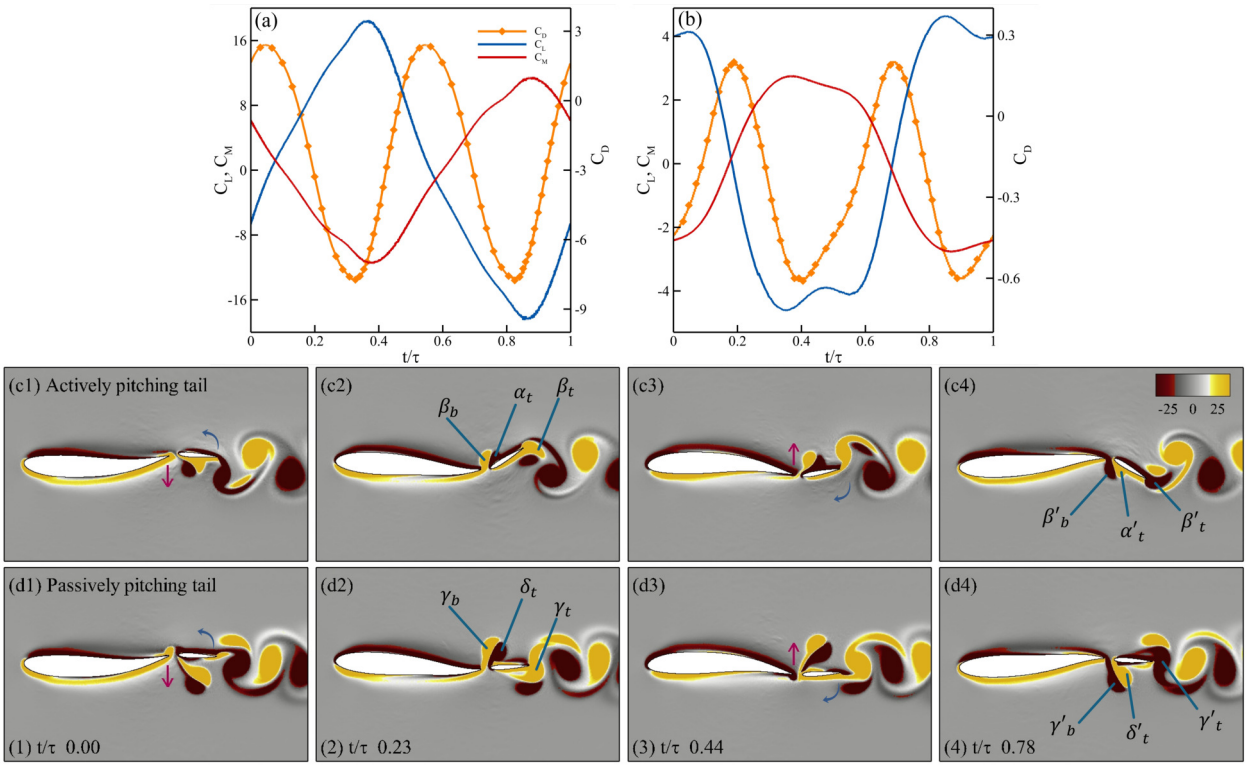

Figure 3.7: Vortex dynamics of actively and passively pitching tails at Re 500 and $f^* = 0.6$. Panels (a) and (b) show the variations of force coefficients C_D, C_L, and C_M over one oscillation cycle for the actively and passively pitching tails, respectively. Panels (c) and (d) depict four characteristic snapshots (1-4) of the flow field for each case, respectively, visualized using contours of z-vorticity corresponding to the same cycle.

In Fig. 3.7(c), panel c1 shows the tail at the start of its downward heaving stroke. In panel c2, a leading-edge vortex (α_t) forms on the upper surface of the tail, producing positive lift and negative drag (i.e., positive thrust). Simultaneously, the tail pitches downward, generating a trailing-edge vortex (β_t), while the body's undulation produces another vortex at the trailing edge of the body (β_b). Due to the effect of β_b, leading to an early formation of α_t which results in the reduction of the pressure on the upper surface. This increase in the pressure differential results in increase in the thrust observed in Fig 3.7(a), similar to the observation drawn by Akhtar et al (46). As the

tail completes its downward stroke (panel c3), it begins to pitch upward and β_t starts to detach from the trailing edge. During the subsequent upward stroke (panel c4), α_t constructively interacts with the newly formed trailing-edge vortex (β_t'), while a new leading-edge vortex develops on the lower surface, resulting in negative lift and negative drag (positive thrust) due to the decrease in the pressure on lower surface.

Figures. 3.7(d1) to 3.7(d4), shows the four instances of the passively pitching tail from panel d1 to d4, respectively. As the tail initiates its downstroke, the lift coefficient decreases (creating downward force) which is in the same direction of the heaving displacement contributing to less power expenditure by the tail. The moment coefficient increases as the tail heaves downward, which leads to the counterclockwise pitching of the tail about its peduncle. As the tail moves downward there is a formation of a larger vortex at the leading edge of the tail (δ_t) and the trailing edge of the body (γ_b). The previously shed vortex from the leading edge of the tail constructively interferes with the trailing edge vortex (γ_t) as seen in panel d2, increasing the strength of this trailing edge vortex. As seen from panel d3, due to the smaller angle of attack of the tail, δ_t does not stay attached to the boundary layer, which leads to the separation of δ_t resulting in the formation of a dipole with γ_b, which is considered detrimental to the production of thrust. When this scenario is compared to the one observed in the actively pitching tail, the formation of the leading edge vortex in both cases leads to the increase in thrust but, with an actively pitching tail, due to the higher angle of attack, the vortex stays attached to the boundary and produces relatively higher thrust. In the same frame, the formation of the trailing edge vortex (γ_t') begins as the tail initiates its upward stroke. In panel d4, the dipole which is formed from γ_b and δ_t breaks as δ_t constructively merges into γ_t' which leads to an increase in thrust.

Based on the earlier analysis, at a Reynolds number of Re =500, 78% of the passively pitching

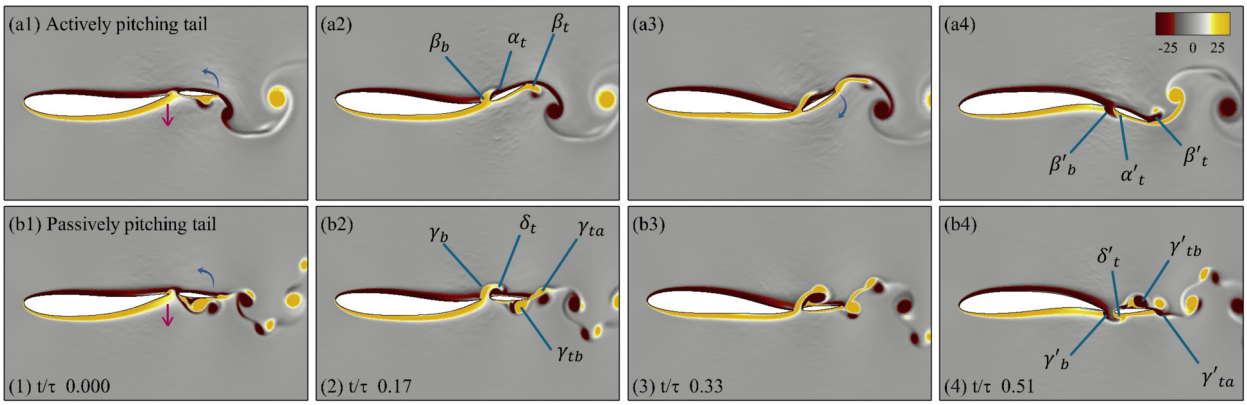

Figure 3.8: Vortex dynamics of actively and passively pitching tails at Re 5000 and $f^* = 0.2$. Panels (a) and (b) depict four characteristic snapshots (1-4) of the flow field for each case, respectively, visualized using contours of z-vorticity corresponding to a half oscillation cycle.

tail configurations outperformed their actively pitching counterparts in terms of power ratio. In contrast, at a higher Reynolds number of Re = 5000, only 38% of the passively pitching tail configurations demonstrated better performance, with most of these cases clustered around a Strouhal frequency of 0.2. Notably, the passive tail configuration with parameters $\zeta = 0.50$ and $J^* = 0.375$ achieved nearly 1.5 times better performance than that of the corresponding active case at the same Strouhal frequency. A comparative analysis of the vortex dynamics over a half oscillation cycle for both cases is presented in Fig. 3.8, shown in comparison.

Figures 3.8(a)–3.8(d) illustrate four key time instances of an actively pitching tail during its downward stroke, corresponding to panels a_1–a_4, respectively. In panel a1, as the tail initiates its downward stroke, a trailing-edge vortex (β_b) begins to form due to the body's undulation. As the tail continues to move downstroke, a leading-edge vortex (α_t) develops on the upper surface of the tail. Simultaneously, as the tail pitches downward about the peduncle, a trailing-edge vortex (β_t) is formed. A key observation between the actively pitching tail at Re = 500 (Fig. 3.7c) and

Re =5000 (Fig. 3.8a) is that while α_t remains attached to the boundary layer in both cases, at the lower Reynolds number, the vortex structure appears more coherent. Contrarily, at Re = 5000, the leading-edge vortex is more tightly bound to the boundary layer, contributing to improved thrust generation. In panel a3, as the tail approaches the end of its downward stroke, the interaction of β_b with α_t produces a jet-like effect, similar to the mechanism described by Gao et al. (1). At this instance, the trailing-edge vortex continues to strengthen as the tail's angle of attack reaches its peak. Panel a4 captures the moment just after the downward stroke ends. Here, the upward pitching of the tail causes the detachment of the trailing-edge vortex β_t, while a new vortex β_t' is formed on the upper surface. The constructive interaction between α_t and β_t' leads to the production of thrust. At this same instant, a new leading edge vortex (α_t') from the tail and a trailing-edge vortex (β_b') from the body appears on the lower surface.

Similarly, Fig. 3.8(b) illustrates the passively pitching tail over a half oscillation cycle as it completes its downward stroke. The four snapshots of this motion are shown in panels b1–b4. In panel b1, as the tail begins its downstroke, a trailing-edge vortex (γ_b) is generated from the undulating body from the lower surface. A core difference between the cases with an actively pitching tail and the passively pitching tail lies in the angle of attack. For the passive tail, the angle of attack does not exceed 6°, which is significantly smaller than 30° observed in the active tail. This reduced angle of attack is consistent across all configurations with the passively pitching tail. However, due to the smaller angle of attack, the leading-edge vortex (δ_t) detaches prematurely from the boundary layer of the tail. As it remains close to the surface, δ_t subsequently reattaches to the boundary layer, as seen in panel b3. Upon reaching the trailing edge of the tail, it sheds as a coherent, clockwise-rotating vortex from the upper surface, relabeled as γ_{tb}'. Such reattachment and delayed shedding help maintain a favorable pressure distribution along the surface of the tail

and promotes the formation of a reverse jet downstream, thereby contributing to the generation of thrust as seen in panel b4. In the same panel, we also observe the formation of a new leading-edge vortex (δ_t') on the tail and a trailing-edge vortex (γ_b') from the undulating body on the lower surface.

The primary contributor to the higher thrust observed in all actively pitching tail configurations is the large angle of attack and a consistent lag between the heaving and the pitching displacement of the tail, which ensures that the leading-edge vortex formed on the tail remains attached to the boundary layer, thereby sustaining thrust generation. A secondary contributor is the constructive interaction between the leading-edge vortex from the first half of the oscillation cycle and the trailing-edge vortex formed in the second half, which further improves the production of thrust. However, this higher thrust comes at the cost of a reduced power ratio. Contrarily, for the passively pitching tail, the smaller angle of attack causes the leading-edge vortex to detach prematurely from the boundary layer of the tail, which is detrimental for the production of the thrust. Nevertheless, when performance is evaluated in terms of power ratio, the passively pitching tail outperforms its active counterpart at Re = 500. At Re = 5000, however, the trend reverses: the actively pitching tail exhibits better performance, particularly at higher Strouhal frequencies, due to the instabilities and inconsistencies observed in the case with a passively pitching tail as discussed earlier.

The configurations with passively pitching tails provide valuable insight for a detailed analysis. Although the pitching amplitude in these cases is comparatively smaller than that of the actively pitching tails, the pitching frequency remains near resonance, as indicated by the spectral compositions of the pitching response of the tail in Figs. 3.9a and 3.9b. The normalized fundamental frequency aligns well with the heaving frequency of the corresponding case, as highlighted by the dashed line.

Overall, the results suggest that smaller swimmers may benefit from passive pitching, while

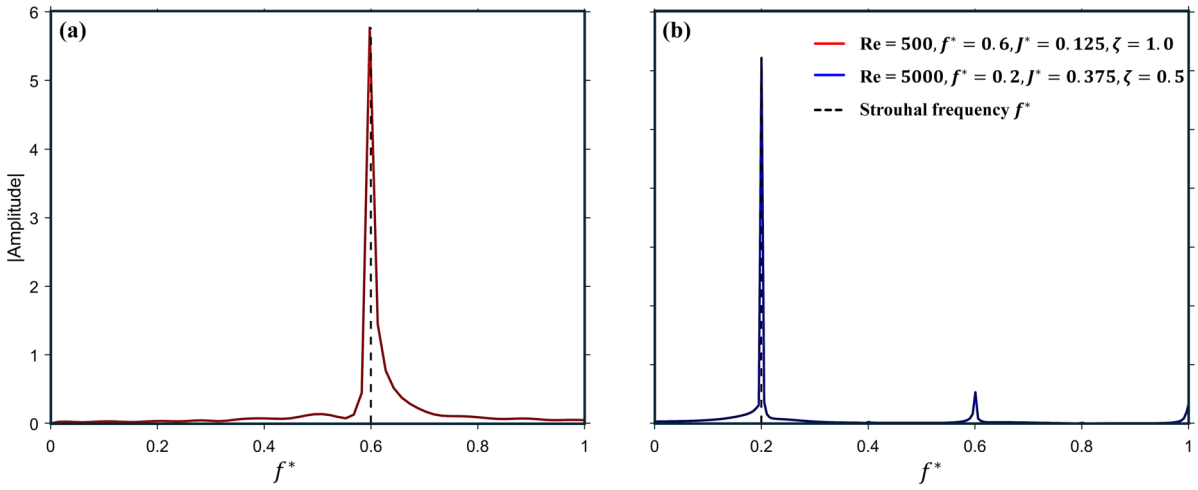

Figure 3.9: Fast Fourier Transform (FFT) of the pitching response of the tail at (a) Re = 500, $f^* = 0.6$, $J^* = 0.125$ & $\zeta = 1.0$, and (b) Re = 5000, $f^* = 0.2$. $J^* = 0.375$, & $\zeta = 0.5$

larger swimmers are more likely to require active pitching mechanisms to maintain optimal hydrodynamic performance.

Chapter 4

3D Investigations of Caudal Fins of Carangiform Swimmers

The kinematic parameters in this chapter are selected to ensure effective simulation plan. Similar to previous section, the wavelength stays unchanged with $\lambda = 1.0$. The Strouhal frequency (f^*), Reynolds Number (Re), inertia, and the coefficient of linear and non-linear stiffness are fixed with their corresponding values shown in Table. 4.1. The damping ratio (ζ). and tuning parameter (n) are varied with an increment of 0.0167, and 2, respectively. It is important to note that the parameters selected in this study are a result of extensive testing of the parameters to land on the variables chosen here.

Table 4.1: Specifications of governing parameters for 3D analysis.

Parameter	Symbol	Value
Undulatory gait	—	Carangiform
Strouhal frequency	f^*	0.3
Wavelength	λ	1.0
Damping ratio	ζ	0.300-0.450
Dimensionless inertia	J^*	3.715
Reynolds number	Re	3000
Tuning parameter	n	42-60
Coefficient of linear stiffness	A	0.85
Coefficient of non-linear stiffness	B	0.15

In our current work, we observe that the linear stiffness acts as a negative recoil term which is responsible for incorporating the pitching with larger amplitude. But, when the pitching approaches a large angle, the cubic non-linear stiffness becomes dominant and triggers the recoil which stabilizes the fin returning it close to the neutral axis. From the test runs, varying n led to tuning the pitching frequency close to the heaving frequency in correlation to the damping ratio. n and ζ yielded 35 simulations and are shown in Fig. 4.1.

Figure 4.1a provides an overview of how n and ζ correspond to the dynamic behavior of the caudal fin. The blue squares indicate asynchronous pitching, characterized by irregular or unilateral pitching. These asynchronous cases are excluded from further analysis in this study. Modes 1–7 represent categories describing how the pitching of the caudal fin evolves with increasing n and

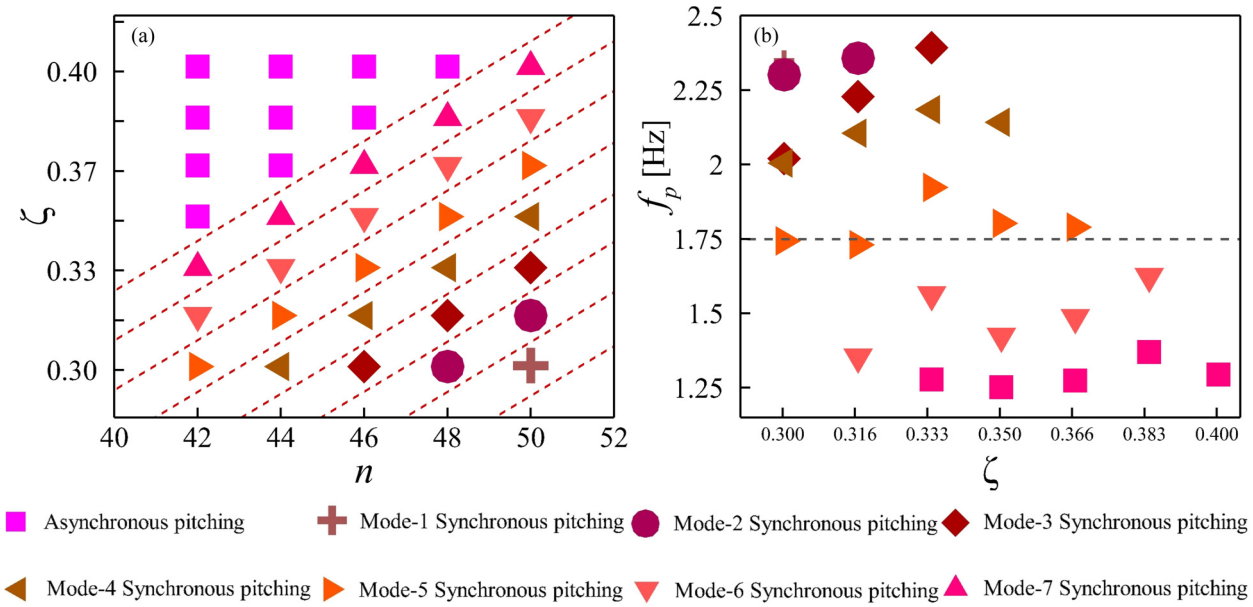

Figure 4.1: Synchronous and asynchronous map for the passively pitching tail with a non-linear stiffness.

ζ linearly. Although simulations within each mode show variations in the fundamental pitching frequency f_p, the discrepancies within a given trend remain relatively small, as illustrated in Fig. 4.1b. This figure shows that, among all simulations performed, fundamental frequency of the simulations from Mode 5 aligns most closely with the undulatory frequency which is highlighted using a dashed gray line across the plot (i.e., 1.75 Hz). Moving away from Mode 5, either by increasing or decreasing ζ, the fundamental frequency of pitching deviates significantly from the undulatory frequency. To investigate this behavior further, we extend the analysis by running an additional set of five simulations following the linear trend of Mode 5, resulting in a total of ten simulations considered for subsequent analysis, the configurations of the simulations are listed in table. 4.2.

From the cases listed in table. 4.2, the steady state response is declared based on the stabi-

Cases	1	2	3	4	5	6	7	8	9	10
ζ	0.300	0.317	0.333	0.350	0.367	0.383	0.400	0.417	0.433	0.450
n	42	44	46	48	50	52	54	56	58	60

Table 4.2: Range of mode-5 synchronous analysis for the pitching of the caudal fin

lization of the pitching frequency of the caudal fin which also corresponds to the fundamental frequency of the pitching. The frequency of each pitching oscillation is recorded and the deviation (Δ) is calculated based on the frequency of the preceding oscillation based on the equation shown below.

$$\Delta = \left| \frac{f_{p_i} - f_{p_{i-1}}}{f_{p_i}} \right| \times 100\% \tag{4.1}$$

Here, f_{p_i} denotes the pitching frequency of the current cycle, and $f_{p_{i-1}}$ is the frequency from the preceding cycle. When the deviation falls within 1%, the cycle is considered stable, indicating that the pitching of the caudal fin has settled and reached its limit cycle. The cycle-by-cycle frequencies for each case, along with their corresponding Δ, are presented in Figs. 4.2a and b, respectively.

In Fig. 4.2a, a clear trend emerges between f_p and ζ. The pitching frequency reaches its steady state value within approximately three oscillation cycles. Cases with lower ζ begin with a significantly reduced initial pitching frequency and gradually increases over successive cycles. In contrast, cases with higher ζ start at frequencies already close to their steady state values. This behavior is further illustrated in Fig. 4.2b, where cases with a low ζ exhibit an initial deviation of nearly 10% from their actual pitching frequency, whereas cases with higher ζ deviate by less than 4%, followed by a rapid drop to below 1%. These observations suggest that, when synchronizing

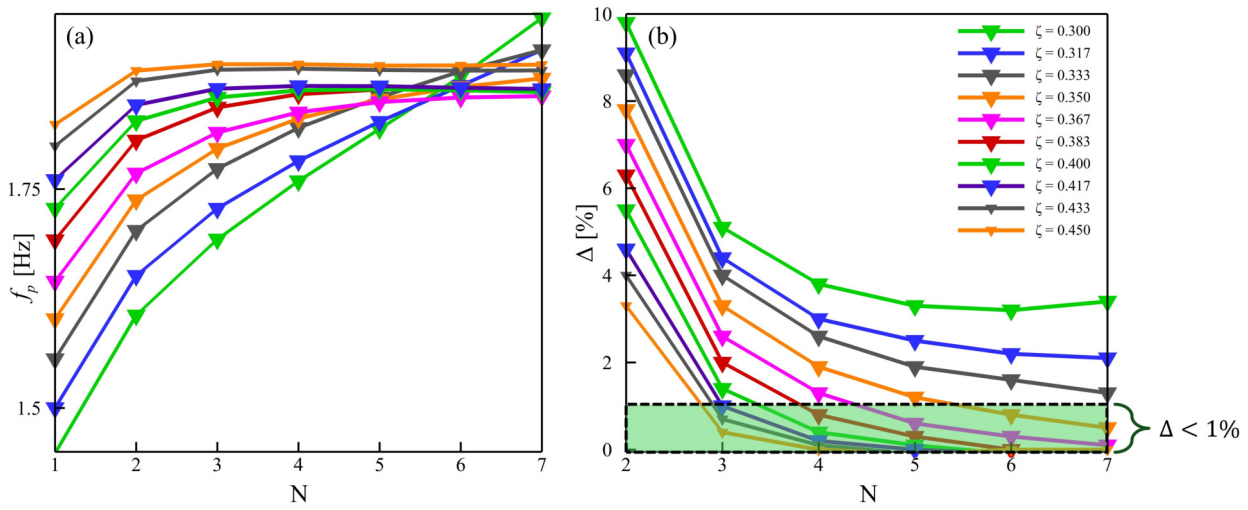

Figure 4.2: The plot shows the (a) cycle-by-cycle pitching frequency of the caudal fin for ζ = 0.300-0.450 with its corresponding tuning parameter n. And the (b) deviation of the frequency to its preceding cycle till it reaches stablility.

the caudal fin with the heaving through a nonlinear stiffness, the system reaches steady state more quickly with an appropriate choice of ζ, allowing accurate prediction of fin behavior from the first oscillation.

To evaluate the performance of the configuration with a passively pitching caudal fin, we construct a reference model with an actively pitching tail. This model ensures that the trailing edge of the caudal fin attains the maximum amplitude, $A(1.0) = 0.1L$, matching the amplitude envelope of a carangiform swimmer, as shown in Fig. 4.3a. The figure illustrates the continuous amplitude distribution along the body of the swimmer, where the caudal fin occupies the region from $x/L = 0.8$ to 1.0 and spans a length of $0.2L$. Figs. 4.3b1 and b5 shows snapshots over a full oscillation cycle for the actively pitching caudal fin. The prescribed pitching is defined by the equation below:

$$\theta_p(t) = f\,(t)\,\sin^{-1}\left\{\frac{1}{c_t}\left[A(1.0)\,\cos\left(2\pi\left(\frac{1.0}{\lambda} - ft\right)\right) - A(0.8)\,\cos\left(2\pi\left(\frac{0.8}{\lambda} - ft\right)\right)\right]\right\}. \tag{4.2}$$

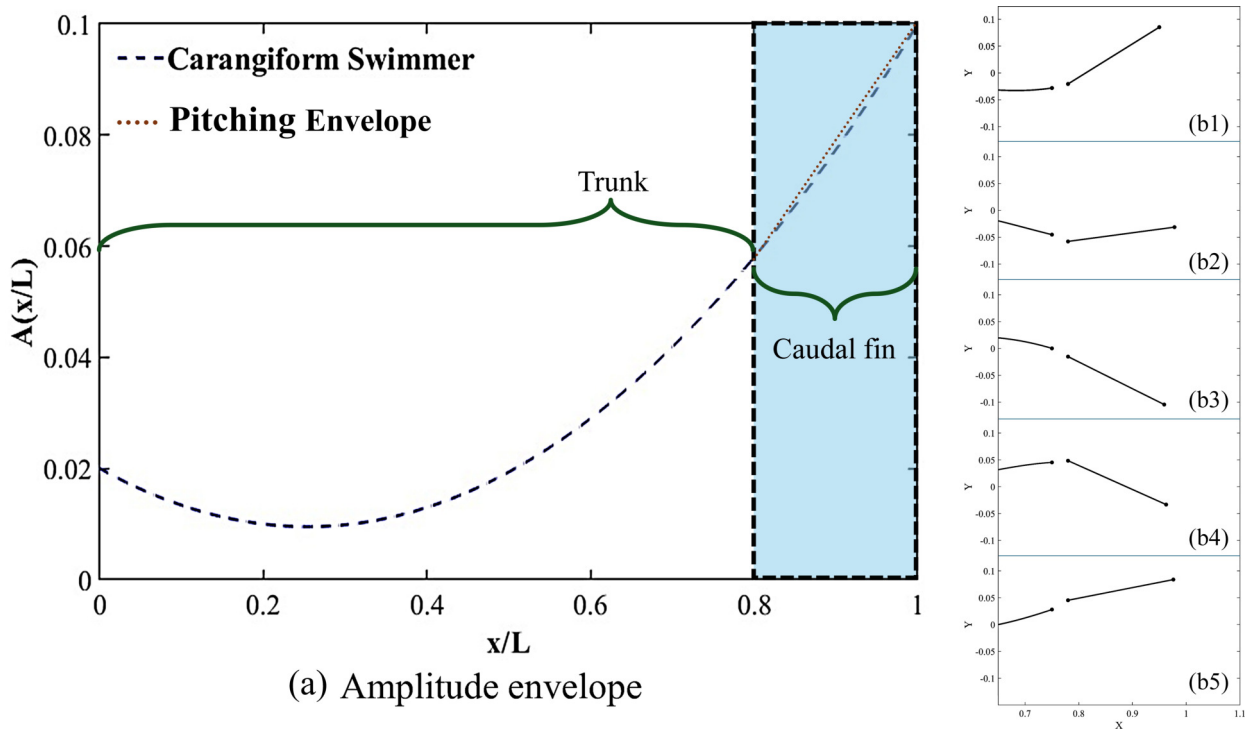

(a) Amplitude envelope

Figure 4.3: Amplitude envelope of carangiform swimmer with (a) undulatory trajectory of the caudal fin alongside its pitching trajectory. (b) represents the active pitching trajectory of the caudal fin over a full oscillation cycle

Where $\theta_p(t)$ represents the pitching angle of the caudal fin, formulated to replicate the characteristic undulation of a carangiform swimmer. The schematic in Fig. 4.3b is derived from the Jackfish model shown in Fig. 4.4 and is used to visualize and analyze the trajectory traced by the caudal fin during swimming. In Fig. 4.4, h denotes the heaving displacement of the caudal fin, while $\theta_p(t)$ indicates its angular displacement.

From the configurations presented in Fig. 4.2, the cases in which the passively pitching caudal fin reaches stability within seven oscillation cycles are examined further. The corresponding angular displacements are plotted in Fig. 4.5. In this figure, $\theta_p(t)$ for all stable cases with passive pitching are displayed alongside a reference line in black line, that represents cases with an actively

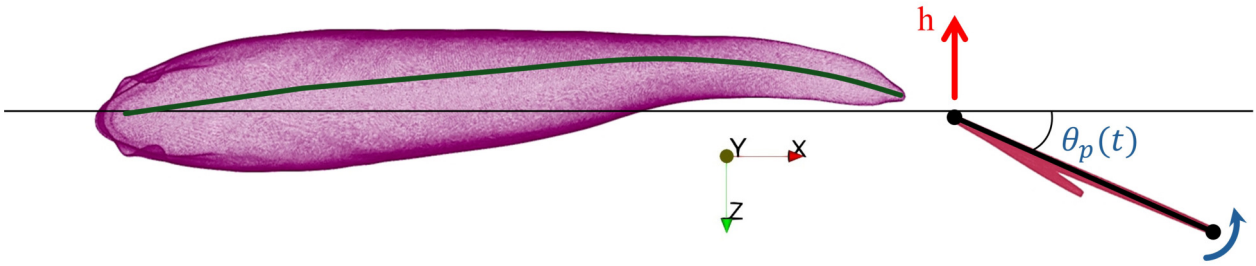

Figure 4.4: Schematic of Jackfish used to represent the pitching of the caudal fin in this study.

pitching caudal fin.

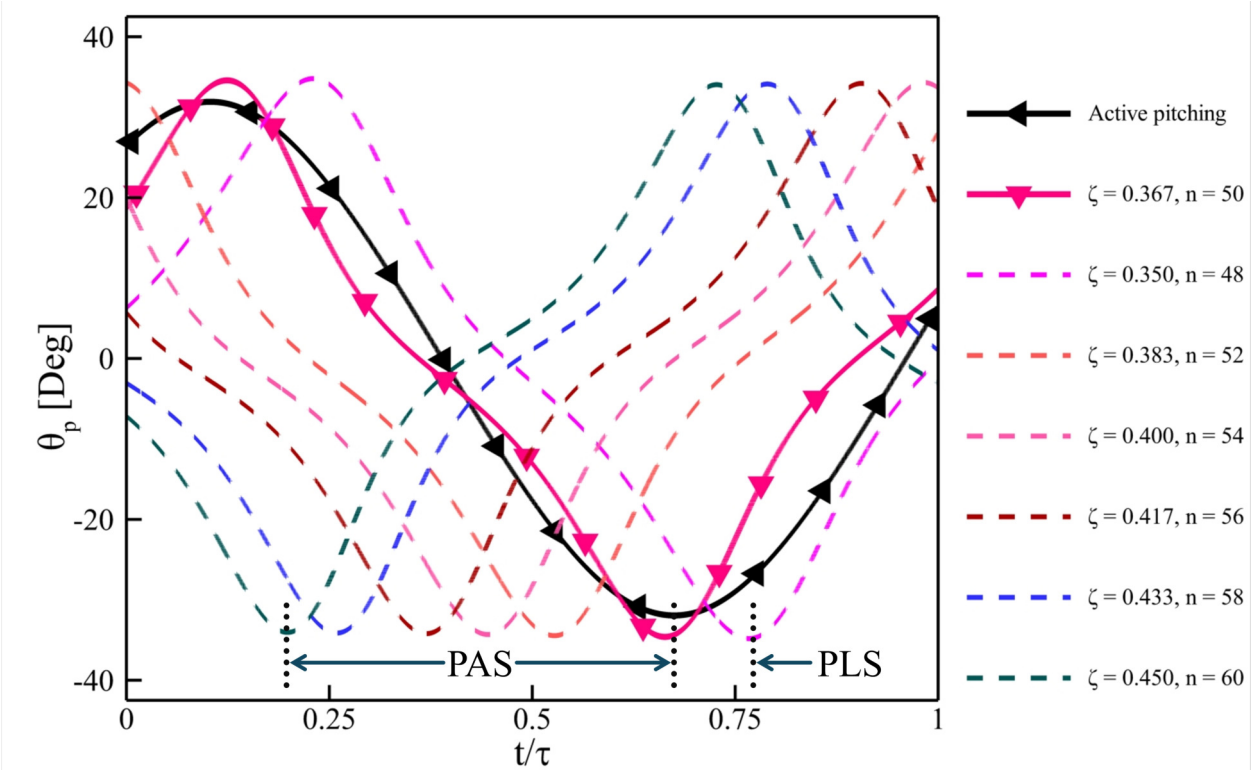

Figure 4.5: Pitching displacement of the caudal fin over a full oscillation cycle for the passively pitching tail alongside its active counterpart.

Among all the cases plotted in the Fig. 4.5, all the configurations with a passively pitching caudal fin shows a distinct behavior than that of the reference case which shows the traditional Sinusoidal wave form with the maximum pitching angle of 32°. The cases with the passively

pitching caudal fin demonstrates a sharp transition in the wave around the peaks which correlates to the nonlinear stiffness stabilizing the system when the pitching approaches a large amplitude, in the configurations shown here all of the cases exhibit the pitching with amplitude larger than 32°. The configuration with the $\zeta = 0.367$, and $n = 50$ demonstrates a very close synchronicity to that of the actively pitching reference case. With the configuration with smaller ζ and larger ζ the the wave tends to display a lag, and advancement (lead), respectively. Phase Lag Synchronization (PLS) is referred to the wave which lags in comparison with the actively pitching case, and Phase Advanced Synchronization (PAS) is referred to the wave which leads in the Fig. 4.5. With increasing the ζ and n the wave exhibits higher PAS. We can analyze the influence that the *PAS* and *PLS* have on vortices being generated in the wake of the swimmer. We plot the dorsal view of the swimmer with all the configurations showed in Fig. 4.5 alongside the actively pitching caudal fin case.

A closer inspection of the wake signatures for all configurations from Fig. 4.5 allows us to compare the dorsal-view wake patterns about the neutral axis for the actively pitching case and cases 4 through 10. The influence of *PAS* and *PLS* on the downstream coherent structures is illustrated in Figs. 4.6a–h. For each case, we report the wake-spread angle θ_s, which quantifies the deviation of the shed vortices from the streamwise direction relative to the centerline of the swimmer. The actively pitching configuration generates a narrow wake with $\theta_s \approx 10°$ (Fig. 4.6a), indicating that the vortices are shed predominantly in the streamwise direction. For the passive cases, distinct trends emerge. In case 4, which displayed a pronounced *PLS* response, the wake-spread angle increases to approximately 16° (Fig. 4.6b), reflecting both a greater lateral displacement of the vortices and a broader spanwise spread. Case 5, whose kinematics most closely resembles the actively pitching fin, produces a comparatively smaller deflection. As we progress from cases 6 through 10 (Figs. 4.6d–h), θ_s increases, correlating with the progressive intensification of *PAS* across these

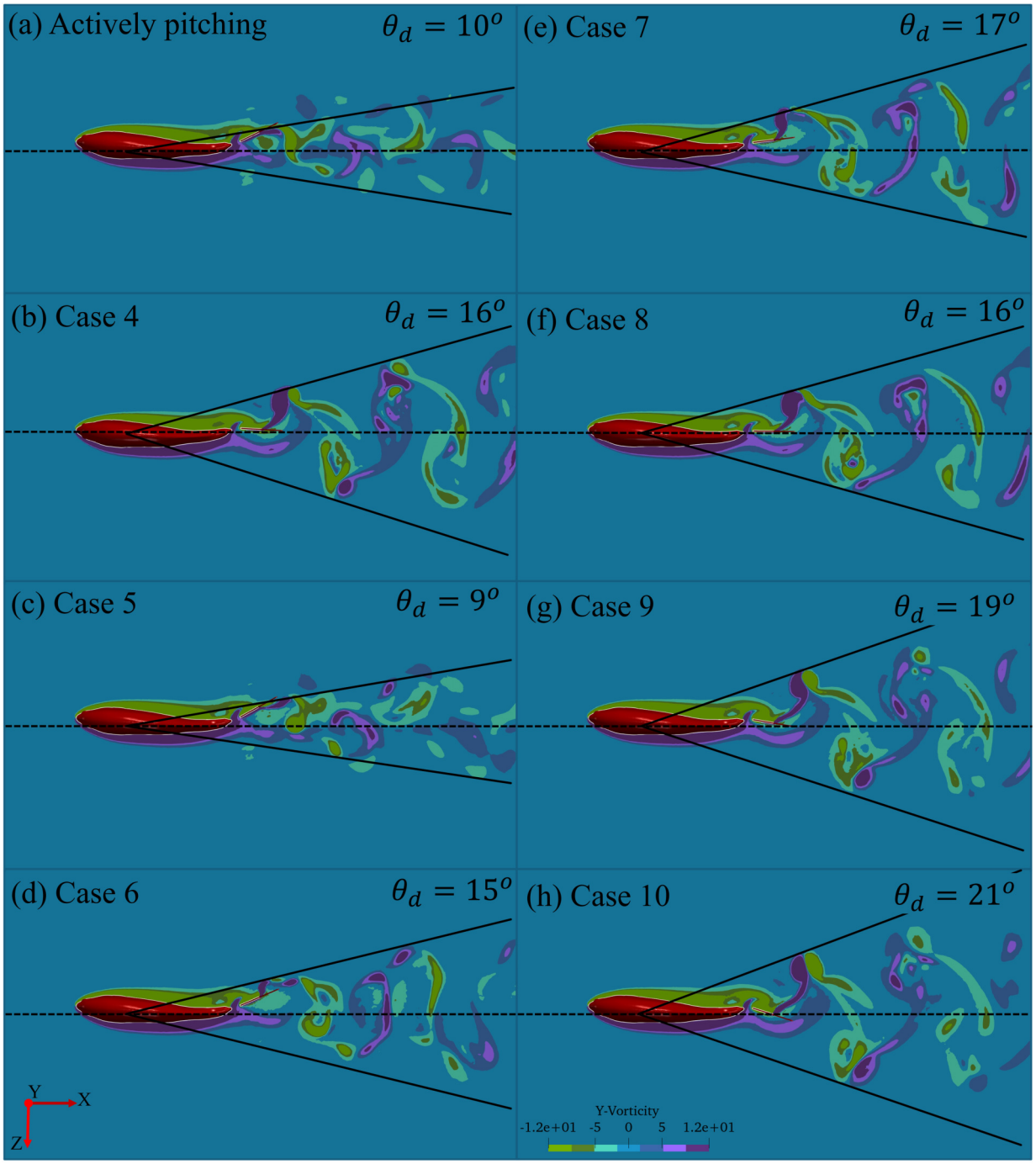

Figure 4.6: Wake signature for all of the configurations from a dorsal view. for (a) an actively pitching tail, alongside (b)-(h) the passively pitching tail for case 4 to 10, respectively.

configurations.

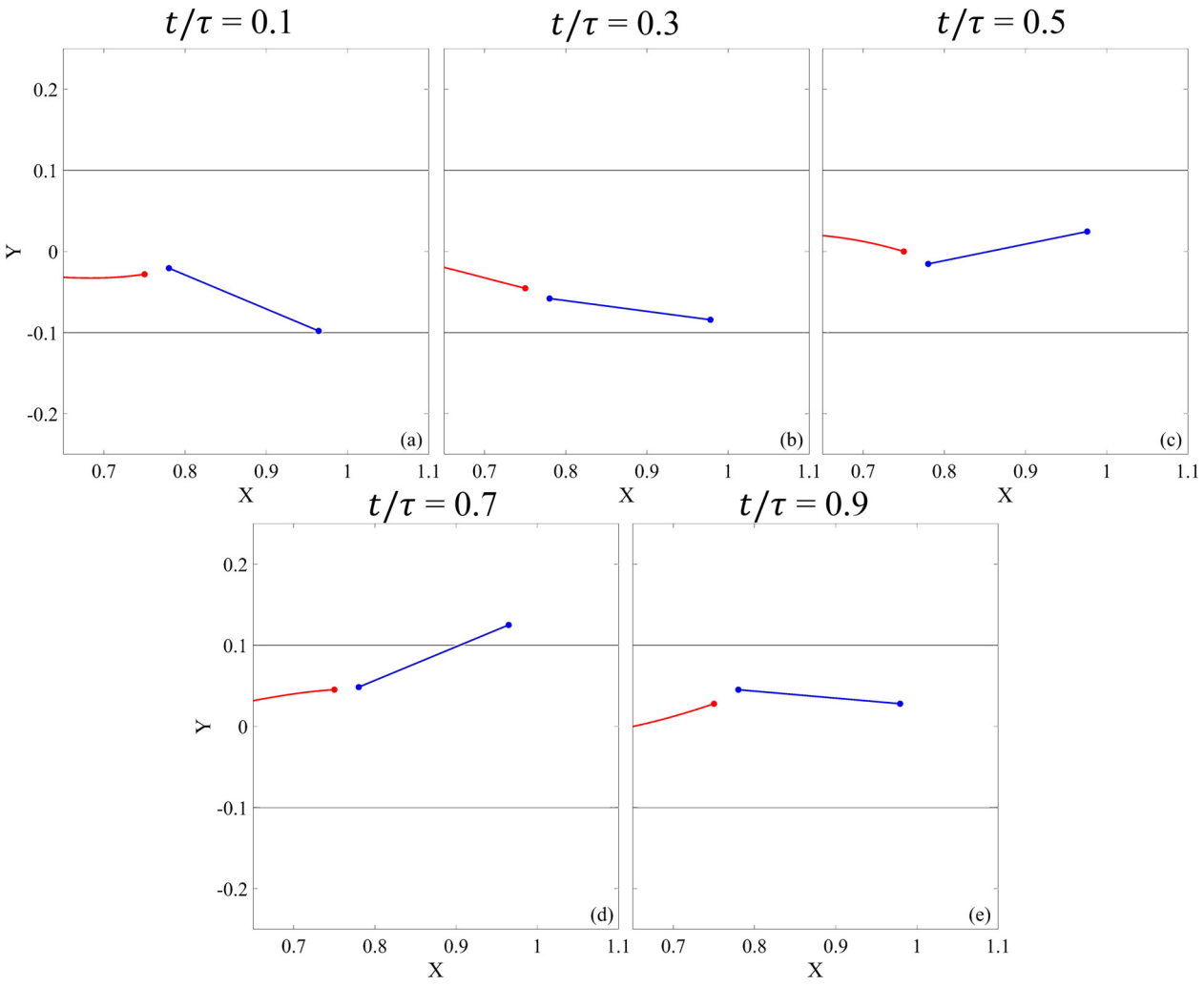

Figure 4.7: Schematic of the case 10 at different stages of its full oscillation cycle.

With increasing PAS, beyond $\zeta = 0.433$ the pitching of the configuration of $\zeta = 0.450$, and $n = 60$ (case 10), the resemblance of the pitching drifts almost into the asynchronous behavior with a large phase between the pitching of the caudal fin and the undulation of the swimmer. The 5 instances over a full oscillation steady state cycle are plotted in Figs. 4.7a to e. In these figures the blue line represents the caudal fin and the circles correspond to the the Leading Edge (LE) and the Trailing Edge (TE) of the trunk and the caudal fin. In these figures, the gray lines are

drawn at $Y = 0.1$, and -0.1, which represents the peak which the TE of the caudal fin achieves in carangiform swimming. In Fig. 4.7c it can be observed that the before the swimmer completes its undulatory cycle, the pitching of the caudal fin has already almost reached to the neutral position, and then has begun the advancement towards its peak of the second half of its oscillation cycle as seen in the Fig. 4.7c and d. In Fig. 4.7d, it can be seen that the caudal fin exceeds the peak to peak amplitude that of a carangiform swimmer.

We now further investigate the performance and the effect of the nonlinear stiffness in a carangiform swimmer, we select the cases which resembles a similar behavior that of an actively pitching tail and a case which largely offsets from the reference case but, still staying in the Synchronized as seen in the Fig. 4.7. We choose the configurations with $\zeta = 0.367$ and $n = 42$ (case 5), and $\zeta = 0.433$ and $n = 58$ (case 9), corresponding to minimal offset and maximum offset from the actively pitching caudal fin, respectively.

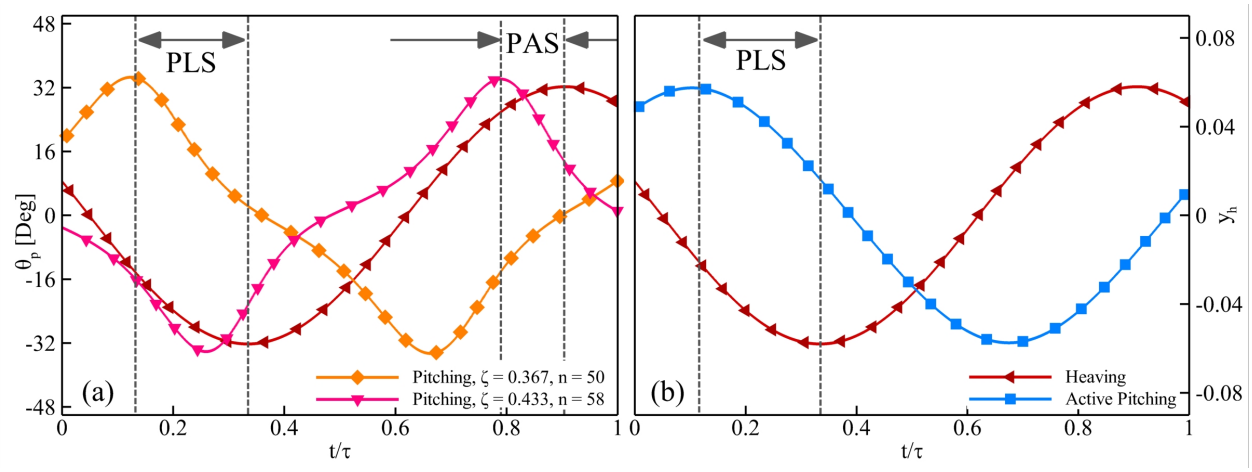

Figure 4.8: The comparison of the heaving and pitching of the caudal fin for (a) passively pitching tail with $\zeta = 0.367$ and $n = 50$, and $\zeta = 0.433$ and $n = 58$ corresponding to case 5, and case 9, respectively. And, (b) Actively pitching tail

Figure 4.8 presents the angular displacement of the caudal fin together with its heaving displacement over one oscillation cycle. The heaving displacement is prescribed such that the leading edge of the caudal fin follows the trajectory of a carangiform swimmer, as discussed earlier. Figure 4.8a illustrates the pitching for cases 5 and 9 alongside the heaving, while Fig. 4.8b shows the corresponding displacement for the actively pitching tail alongside its heaving . In case 5, the pitching displacement lags behind the heaving, which closely resembles the phase lag observed in the actively pitching case shown in Fig. 4.8b, indicating the presence of a *PLS*. Conversely, the pitching in case 9 exhibits a *PAS*, which is notably distinct from the actively pitching configuration. To

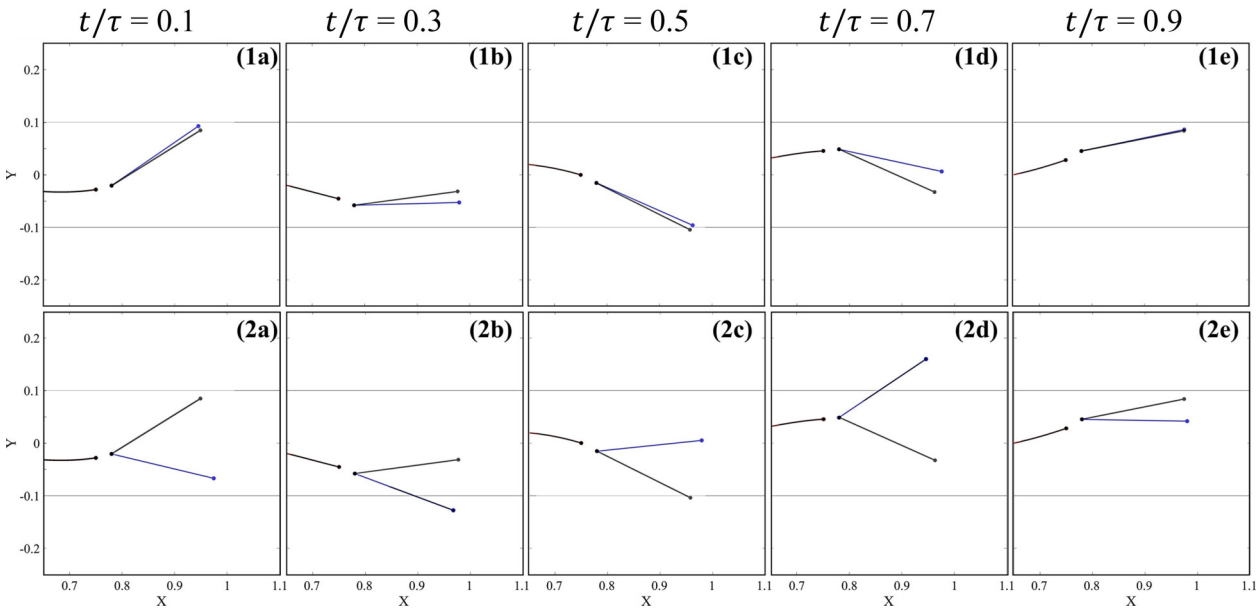

Figure 4.9: Schematic of the (1a)-(1e) case 5, and (2a)-(2e) case9 9 at different stages of its full oscillation cycle. In comparison with the schematic of the actively pitching case in black.

The pitching oscillations of cases 5 and 9 are illustrated at five distinct instances over one com-

plete oscillation cycle. In Fig. 4.9, the caudal fin undergoing passive pitching is shown by the blue line, whereas the actively pitching trajectory is shown in black. Case 5, in Fig. 4.9(1a)–(1e), exhibits a close agreement between the passive and active pitching throughout the cycle. The primary deviation occurs near the neutral axis, consistent with the phase disparity observed earlier in Fig. 4.5. Furthermore, for both passive and active configurations, the TE traverses the same peak-to-peak amplitude envelope of a carangiform swimmer. In contrast, case 9 demonstrates a pronounced deviation between the two pitching. The passively pitching caudal fin reaches and departs from its peak positions abruptly, advancing ahead of the heaving. This sharp recoil decelerates as the fin approaches the neutral axis, resulting in a reduced phase difference between the passive and active pitching, as illustrated in Figs. 4.9(2b), (2c), and (2e). The pitching of cases 5 and 9 exhibit a comparable recoil behavior near the peak displacement, which exerts a dominant influence on both the thrust coefficient ($-C_D$) and the moment coefficient (C_M), as observed in the subsequent analysis.

The analysis of the moment and drag coefficients (C_M and C_D) presented in Figs. 4.10a and b, respectively, provides deeper insight into the fluid–structure interaction of the caudal fin. As shown in Fig. 4.10a, the C_M amplitude for case 9 is markedly higher than that of case 5 and the actively pitched configuration. Although case 5 exhibits a smaller C_M compared to case 9, it remains higher than the actively pitching tail. Both passive and active pitching displays pronounced spikes in C_M around the instant when the caudal fin abruptly recoils from the peak position. In Fig. 4.10b, the variation of C_D reveals that case 5 exhibits a thrust-dominant response, whereas the actively pitched caudal fin maintains a nearly symmetric profile. Conversely, case 9 exhibits large amplitude fluctuations in C_D, with the waveform remaining predominantly within the positive C_D range, indicative of a drag-dominated behavior. These observations suggest that the passively pitching

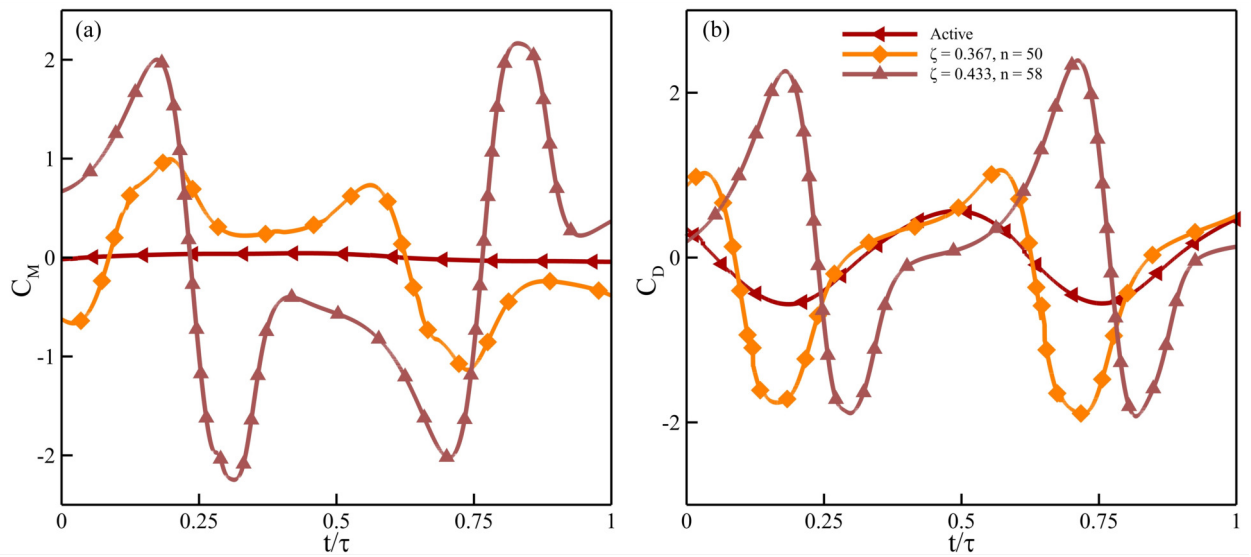

Figure 4.10: (a) Moment coefficient (C_M), and (b) Drag coefficient (C_D) Comparison between the case 5, case 9, and the actively pitching tail over an oscillation cycle.

configuration in case 5 offers a hydrodynamic advantage over both the highly asynchronous case 9 and the actively pitching counterpart. The contrast in C_M and C_D suggests distinct vortex shedding and LEV/TEV coherence across cases, prompting an analysis of the near-wake structure and its phase relation to the motion of the caudal fin.

To facilitate a clear and consistent interpretation of the hydrodynamic mechanisms underlying these coefficient trends, a schematic representation of the caudal fin and associated terminology is provided in Fig. 4.11. This illustration describes the upper and lower lobes of the bi-lobed caudal fin, the right ventral and left ventral sides, and the heaving displacement. Establishing this nomenclature is essential for maintaining clarity in subsequent discussions, particularly when describing vortex formation, detachment, and their spatial relationship to the surface of the fin. By standardizing the reference frame and labeling conventions, the schematic ensures that the interpretation of the wake structures and their phase alignment with the fin kinematics is both

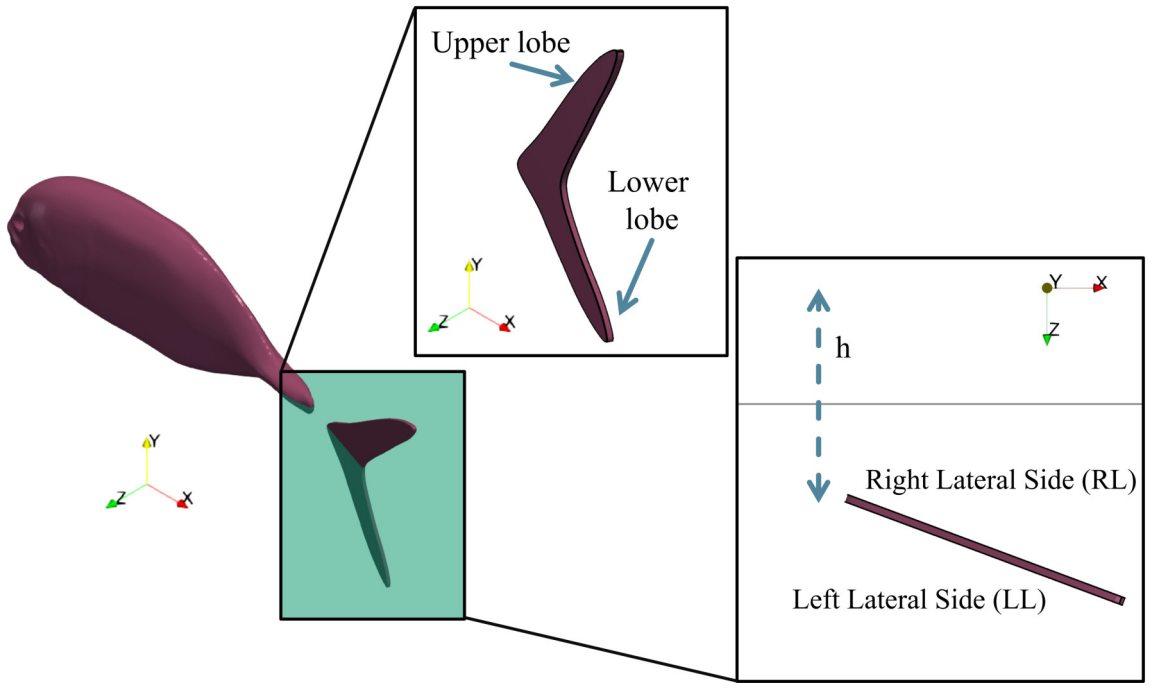

Figure 4.11: Nomenclature used to track the vortices developed and sheded from the caudal fin of the Jackfish

precise and unambiguous.

As observed earlier in Fig. 4.8, the pitching displacement in case 5 closely resembles that of the actively pitching configuration. However, a key distinction emerges in the recoil–advance behavior in the passive pitching. The passively pitching tail undergoes an asymmetric transition as it departs from the peak position, whereas the actively pitched tail follows a smooth, sinusoidal trajectory. This asymmetric response of the stiffness plays a significant role in the generation of thrust in the passive pitching configuration.

Figure 4.12a–f presents the vorticity contours for case 5 over half of an oscillation cycle, during which the caudal fin pitches from the left ventral side toward the right ventral side. The pitching can be divided into two distinct phases. Phase 1 (t/τ = 0.1–0.3) corresponds to the fin

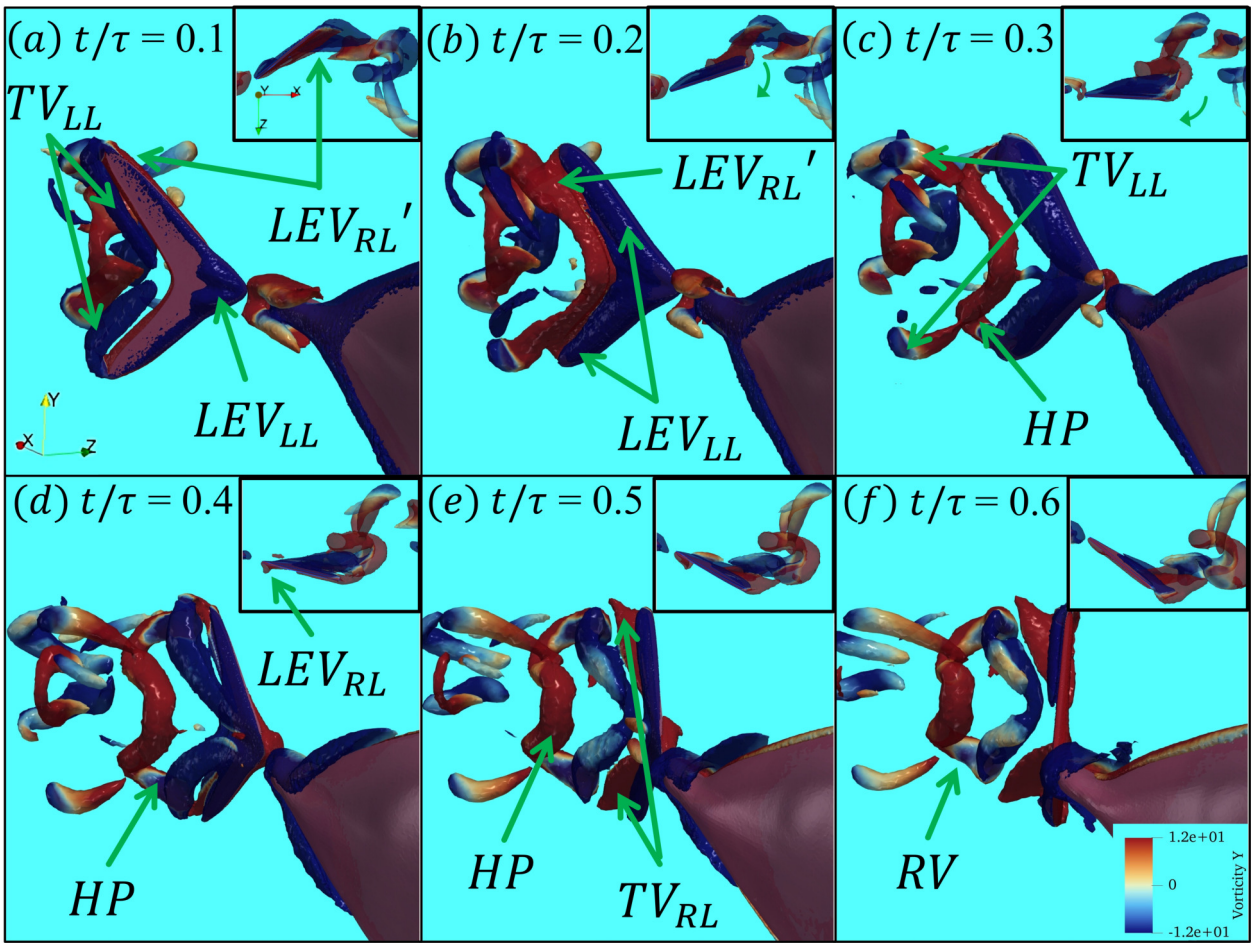

Figure 4.12: Plot showing the closeup vortices generated and sheded in a half oscillation cycle (a)-(f)from the caudal fin of the Jackfish for case 5. Plot shows the iso-surface of $Q = 40$ colored by the range of y-vorticity.

pitching from the left ventral side toward the right ventral side as it approaches the neutral axis. Phase 2 (t/τ = 0.4–0.6) begins once the fin crosses the neutral axis and continues as it gradually pitches toward the peak on the right ventral side. In Fig. 4.12, each snapshot includes a dorsal view inset in the upper right corner, which assists in tracking the instantaneous orientation of the fin and examining the evolution of vortical structures on the right ventral side. The vortices in the isometric view are visualized using a Q-criterion threshold of 12, while the dorsal view employs

both $Q = 12$ and a translucent $Q = 8$ to highlight coherent structures.

Figure 4.12a captures the instant immediately after the caudal fin begins its pitching stroke from the left ventral side towards the right ventral side. At this stage, tip vortices (TV_LL) forms at both the upper and lower lobes, and a leading-edge vortex (LEV_LL) develops on the left ventral side. Meanwhile, the leading-edge vortex on the right ventral side from the previous cycle (LEV_RL) remains attached to the fin surface. Advancing to the next instance in Phase 1, shown in Fig. 4.12b, the remnant leading-edge vortex (LEV_RL') on the right ventral side convects downstream and around the trailing-edge span of the fin, while LEV_LL continues to strengthen on the left ventral side and the tip vortex (TV_RL) on the same side sheds into the wake. In Fig. 4.12c, the upper and lower tip vortex have clearly detached into the wake. The convected LEV_RL', which rolls downstream along the trailing-edge span before detaching, stretches into a structure that mirrors the geometry of the trailing-edge span and remains connected to LEV_LL through the upper and lower lobes. This combined structure closely resembles a hairpin vortex (HP). As noted earlier in Fig. 4.8, the caudal fin pitches away from its peak amplitude rapidly, promoting the formation of this hairpin vortex. The resulting HP morphology is influenced by the geometry of the fin, and in this case, it adopts the characteristic curvature of the trailing-edge span.

Moving into Phase 2, the pitching of the caudal fin slows as it crosses the neutral axis and approaches the end of the half-stroke, where it reaches its maximum heaving amplitude. In Figs. 4.12d–f, a portion of the left ventral-side vortex (LEV_LL) begins to detach from the surface while remaining connected to the hairpin vortex (HP) through the upper and lower lobes. The dorsal-view insets show the emergence of a new leading-edge vortex (LEV_RL) from the right ventral side as the angle of attack increases. The gradual pitching in this phase prevents a complete separation of LEV_LL, a feature known to mitigate thrust loss. In Fig. 4.12e, LEV_RL strengthens

while remaining attached to the right ventral side of the fin. At the same time, the previously formed HP, which had remained connected to $LEV_L L$, fully detaches from the fin and stretches into a distorted ring-like coherent structure. As the angle of attack continues to rise, new tip vortices emerge from the upper and lower lobes on the right ventral side. In Fig. 4.12f, the distorted structure observed at the earlier instant evolves into a more complete ring vortex, once again adopting a geometry that closely follows the shape of the trailing-edge span of the caudal fin.

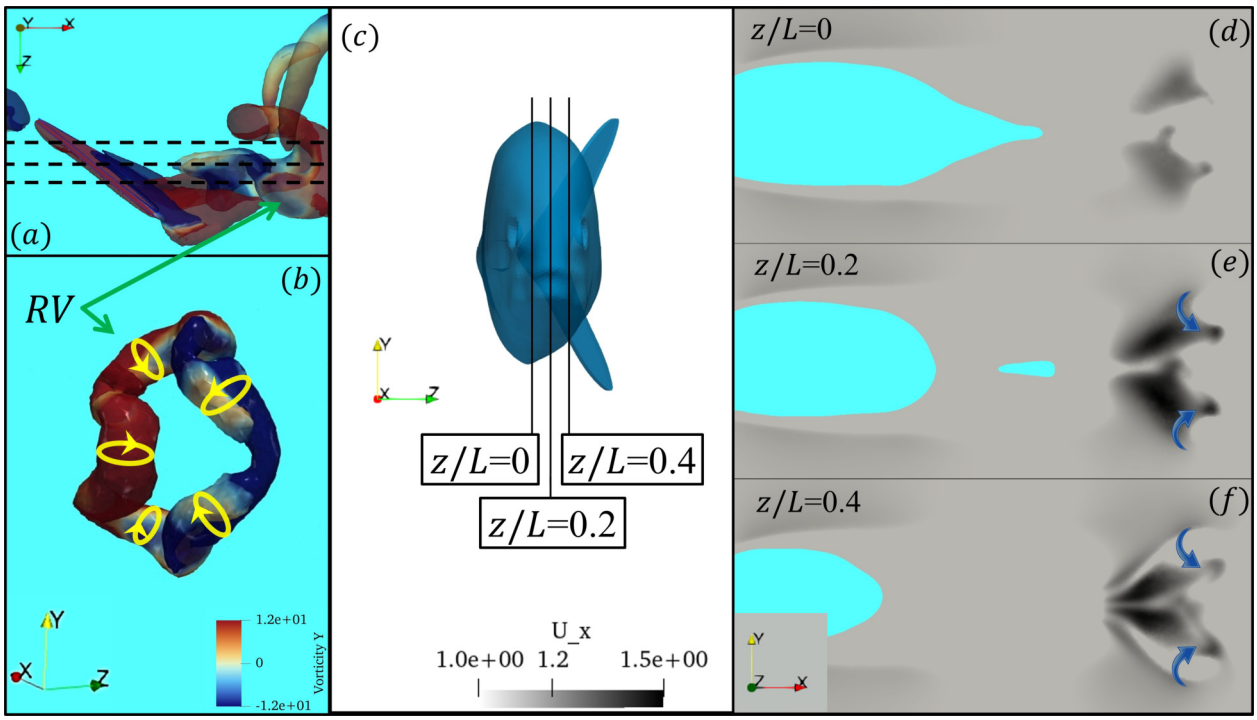

Figure 4.13: This figure presents the ring vortex generated in case 5 at $t/\tau = 0.6$, shown from (a) the dorsal view and (b) the isometric view. Image (c) indicates the locations of the iso-surface slices along the z-axis from the anterior view of the swimmer, corresponding to images (d)–(f), which display the streamwise velocity contours extracted from each slice.

We can examine the influence of the ring vortex observed in Fig. 4.12f using the instantaneous streamwise velocity distribution. Fig. 4.13a presents the dorsal view of the caudal fin, showing

the geometry of the ring vortex in the X–Z plane along with the three dashed lines that indicate the locations of the slices used for the illustration for the velocity analysis. The anterior view in Fig. 4.13b further clarifies the spatial placement of these slices relative to the fin. Velocity contours extracted from the Y–Z planes at $z/L = 0$, 0.2, and 0.4, shown in Figs. 4.13d, e, and f, respectively, display the streamwise velocity in the range $U_x = 1$ to 1.5 (normalized as $\dot{U}x = \dot{x}/U\infty$). Figure 4.13c isolates the ring vortex, where the red color contour represents the anti-clockwise rotation of the vortex about Y-axis and the blue color shows the clockwise rotation of the vortex.The inward folding ring implies an increase in the spanwise velocity as the vortex sheds downstream. Examining Figs. 4.13d–f, a clear jet-like effect is observed in the wake at the instant where the ring vortex is formed. In slice (e), the streamwise velocity peak is most pronounced, corresponding to the center region between the upper and lower lobes of the ring vortex, where its inward-directed rotation contributes to the streamwise momentum.

To contextualize the thrust-dominated behavior discussed earlier, we next examine the dorsal-view vortex dynamics at the end of a full oscillation cycle ($t/\tau = 0.9$) for the actively pitching case, case 5, and case 9, shown in Figs. 4.14a–c, respectively. These snapshots allow the fin posture to be visually correlated with the vortical structures present in the wake. In Fig. 4.14a, the actively pitching configuration sheds two tip vortices from the right ventral side (TV_RL) and two from the left ventral side (TV_LL) over one cycle. We can see the LEV_RL form on the caudal fin, and a hairpin vortex emerges from the trailing-edge span. This hairpin structure reflects the geometry of the fin, with distinct upper and lower lobes, which then stretches downstream to form the tip vortices observed in the wake. In Fig. 4.14b, case 5 exhibits the ring vortices previously analyzed, with their inward rotational direction clearly visible and contributing to the strengthening of the downstream jet associated with thrust production. In contrast, Fig. 4.14c for case 9 reveals several

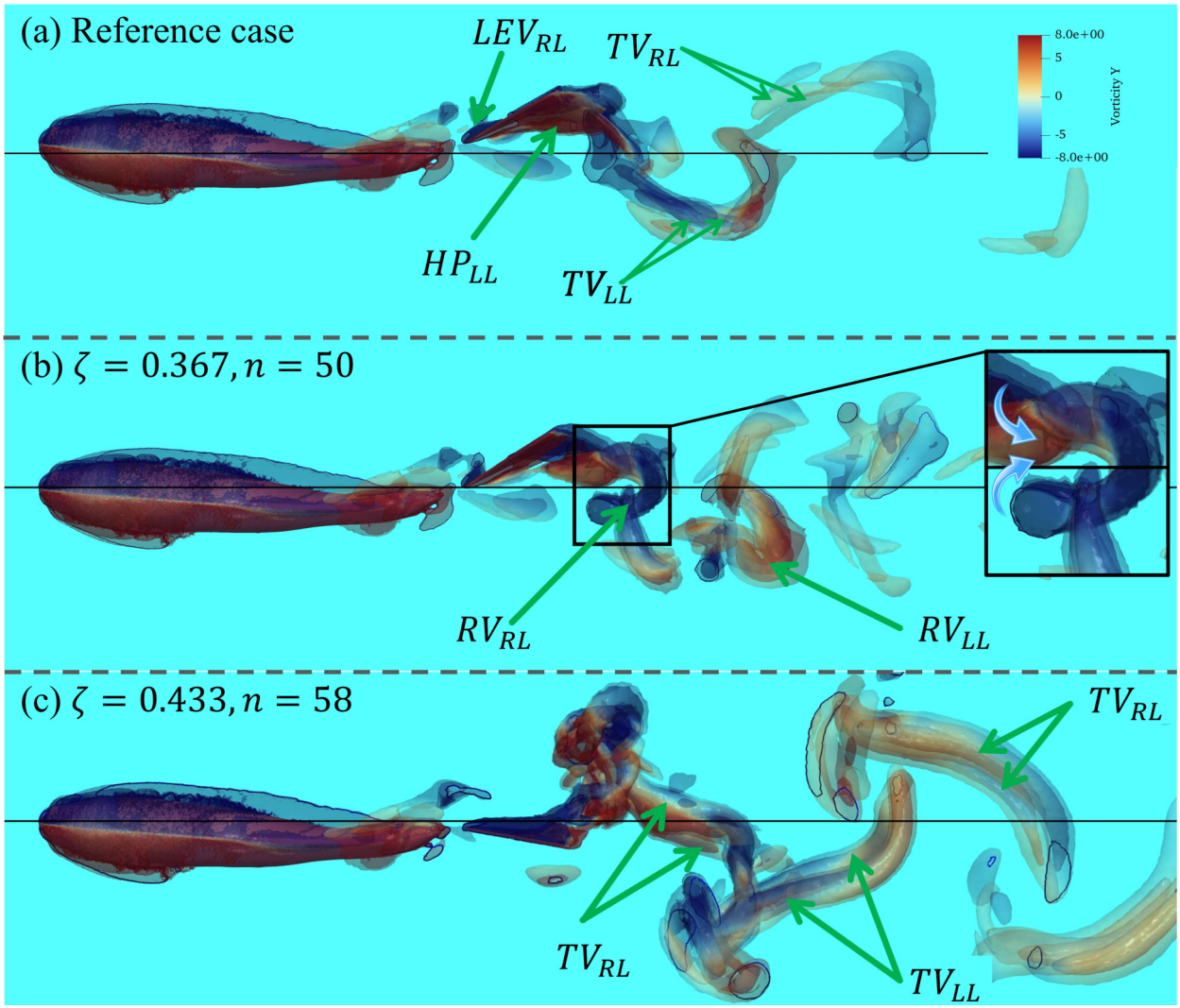

Figure 4.14: y-Vorticity contours corresponding to the swimmer from the dorsal view at the end of an oscillation cycle for (a) case with an actively pitching tail, (b) case 5, and (c) case 9. Plot shows the iso-surfaces at $Q = 40$, and translucent $Q = 8$.

notable features. First, the pronounced *PAS* is evident from the larger displacement of the caudal fin relative to both the active configuration and case 5. Second, the wake pattern contains two right ventral-side and two left ventral-side tip vortices—similar to the active case, yet the spatial distribution differs. The vortices in case 9 display significantly greater lateral spreading, indicating a broader wake footprint compared to the actively pitching fin.

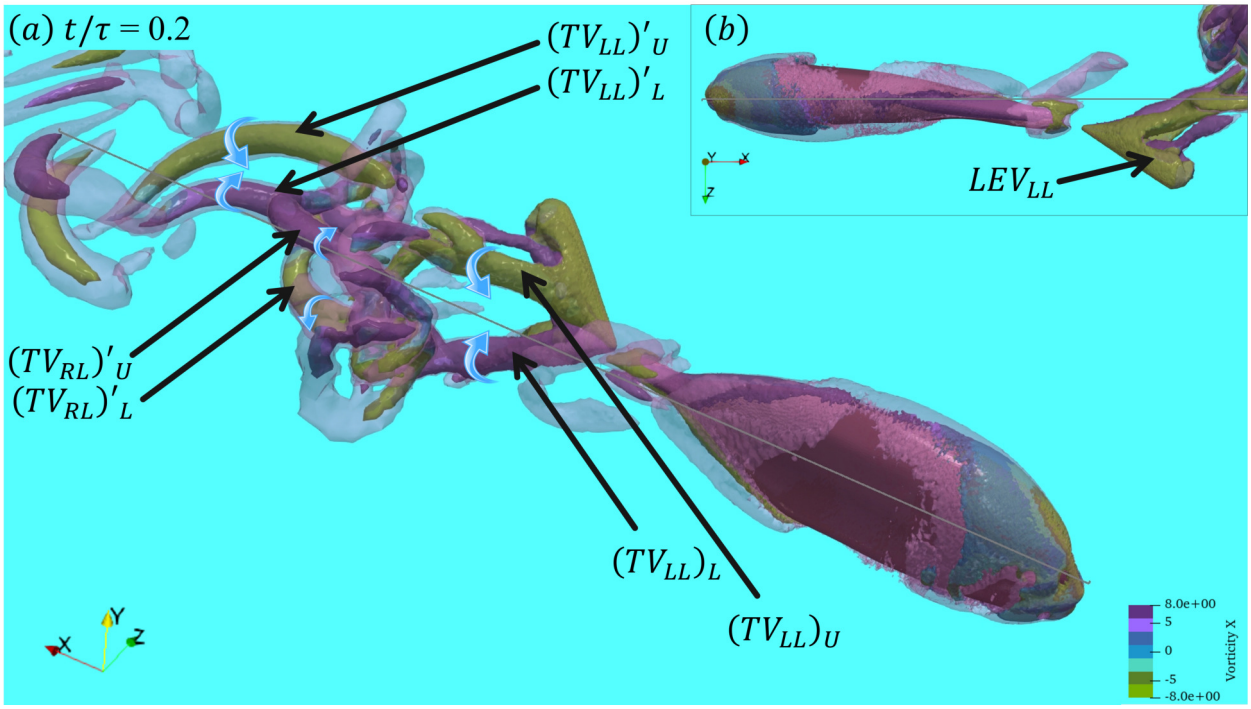

Figure 4.15: x-Vorticity contours corresponding to the swimmer from the (a) iso-matric view, and (b) the dorsal view at the end of an oscillation cycle with the iso-surfaces at $Q = 40$, and translucent $Q = 8$

Figure 4.15a presents the isometric view of the swimmer, while Fig. 4.15b shows the corresponding dorsal view, visualized using Q-criterion thresholds of 50 and 10. The coherent structures in the wake display strong extension in the streamwise direction, motivating the use of x–vorticity contours to characterize them. In Fig. 4.15a, the tip vortices shed from the caudal fin are evident; however, unlike cases where the vortices originate at the trailing-edge span, these structures detach directly from the left ventral-side leading-edge vortex (LEV_LL) as it forms and separates from the surface. The previously shed vortices are labeled as $(TV_RL)'_U$ and $(TV_RL)'_L$ for the upper and lower right ventral-side vortices, and $(TV_LL)'_U$ and $(TV_LL)'_L$ for their left ventral-side counterparts.

The newly formed left ventral-side vortices, $(TV_LL)_U$ and $(TV_LL)_L$, appear as the angle of at-

tack increases, indicating a premature separation of the left ventral-side vortex. Such early detachment is typically associated drag. Examination of their rotational direction shows inward rotation, similar to what was observed in case 5. However, in case 9, this inward rotation induces a more pronounced spanwise spreading of the vortex, in contrast to case 5 where the ring vortex strengthened the streamwise jet. Here, the dominant lateral influence suggests that the vortex dynamics favor wake broadening rather than axial velocity.

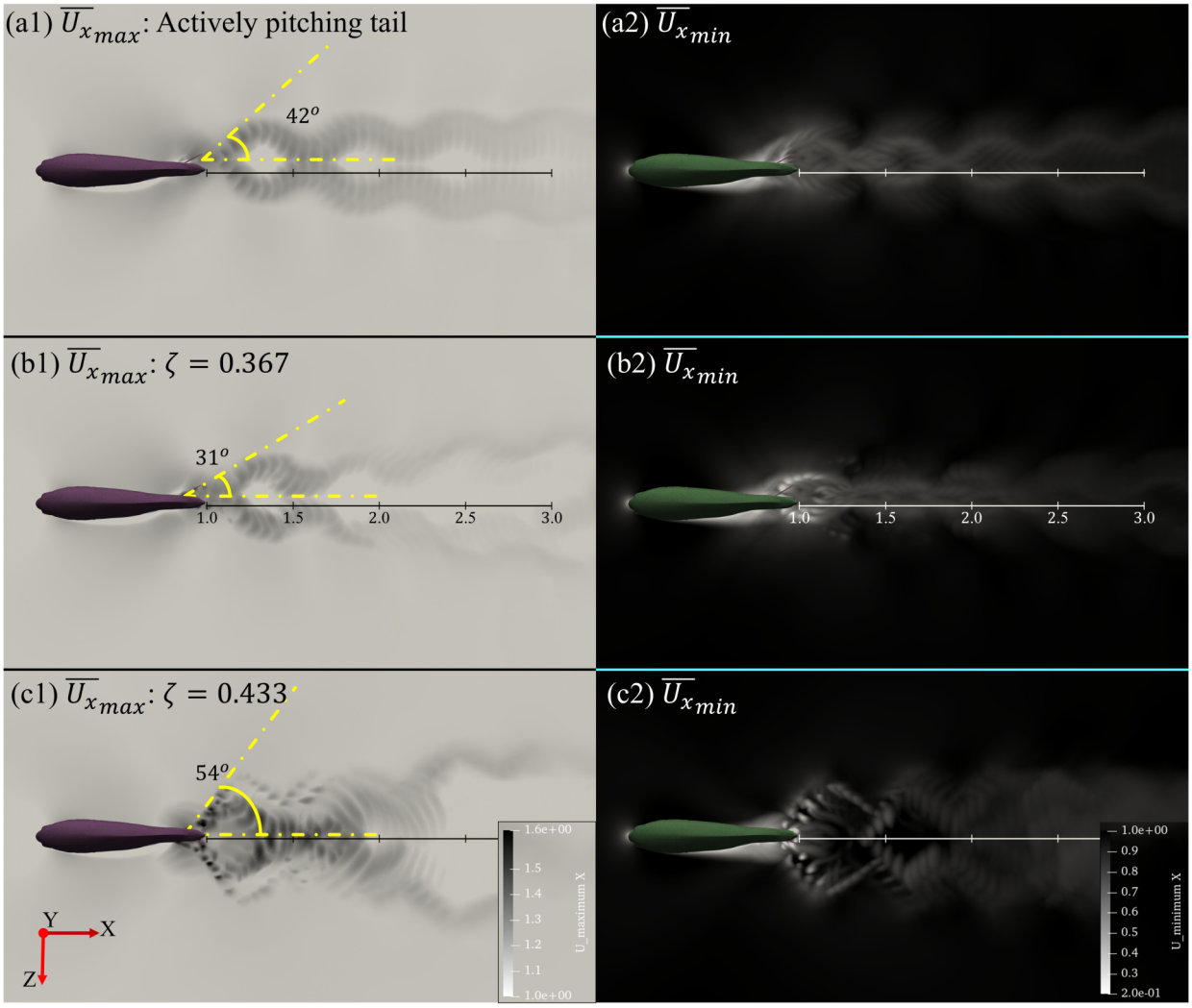

Figure 4.16: Iso-surface shows the cycle-averaged value for the case with ($a1$ & $a2$) an actively pitching tail, ($b1$ & $b2$) case 5, and ($c1$ & $c2$) case 9 referring to $\overline{U_{xmax}}$, $\overline{U_{xmin}}$, respectively.

Figure 4.16 shows the contours of the maximum and minimum cycle-averaged streamwise velocity for the actively pitching case, case 5, and case 9, presented in Figs. 4.16a(1–2), b(1–2), and c(1–2), respectively. Figs. 4.16$a1$, $b1$, and $c1$ correspond to the maximum cycle-averaged streamwise velocity, while Figs. 4.16$a2$, $b2$, and $c2$ present the corresponding minimum values. For the actively pitching fin, the $\overline{U_x}$max distribution exhibits a well-defined diverging jet, forming an inclination angle of approximately 42° with the centerline. The contours gradually weaken downstream, reflecting the decay of streamwise momentum. In contrast, the $\overline{U_x}$min field in Fig. 4.16($a2$) displays a narrow wake footprint that highlights regions of reduced velocity relative to the freestream. This low-velocity region dissipates rapidly, indicating that the associated vortical shedding exerts a neutral influence and do not contribute significantly to thrust or drag.

In Fig. 4.16($b1$), case 5 shows a jet inclination angle of approximately 31°, smaller than that of the actively pitching fin but with a wake pattern that closely resembles it. The $\overline{U_x}$min field in Fig. 4.16($b2$) reveals an even narrower and weaker region of reduced velocity, consistent with the strong thrust observed for this configuration. In contrast, case 9 exhibits the largest jet inclination angle, reaching nearly 54° in Fig. 4.16($c1$). Although a strong streamwise jet persists up to roughly $2.0L$, the wake bifurcates beyond this distance. Examination of Fig. 4.16($c2$) shows that $\overline{U_x}\text{min} < U_\infty$ near the centreline, producing a low-momentum region associated with reduced thrust. This behavior aligns with the broader, more diffused wake generated by the pronounced *PAS* in case 9. As discussed by Dong et al. (47), and observed in this study, the larger jet inclination angle correlates to the drop in thrust.

4.1 Summary

This study establishes that nonlinear stiffness in the peduncle decisively governs the $3D$ kinematics and hydrodynamic performance of a swimmer with a passively pitching caudal fin. The displacement-dependent stiffness enables large angular excursions while maintaining stability at extremes, leading to a natural recoil in which the rapidly increasing restoring moment near peak pitch drives the fin back toward its neutral position. This produces amplified pitching and a clear phase shift relative to the heaving, arising solely from fluid–structure interaction, without any prescribed pitching kinematics.

The nonlinear recoil mechanism strongly influences vortex formation in the wake, promoting the shedding of coherent ring-like and hairpin-like vortices that contribute to propulsion. These structures generate a focused downstream momentum jet, yielding improved thrust when compared to a system with an actively pitching tail.

Overall, the results demonstrate that non-linear peduncle stiffness functions as a hydrodynamically advantageous mechanism, regulating amplitude, phase, recoil, and vortex dynamics. The resultant passive kinematics capture key characteristics of actively pitching caudal fins while sustaining strong thrust production, emphasizing the significance of stiffness modulation in biological peduncles and offering a pathway for bio-inspired propulsion systems based on passive synchronization rather than active pitching.

Conclusions and Future Work

4.2 Conclusions

Across the two studies presented in this thesis, the fundamental question has been how the caudal fin of an undulating swimmer responds with actively pitching tail or emerges passively through fluid–structure interaction. Although the two studies employ different modelling frameworks, dimensionality, and parameter spaces, they collectively highlight the rich interplay between structural design, stiffness characteristics, and hydrodynamic performance of the swimmer with a passively pitching tail.

The first study establishes a comprehensive two-dimensional foundation by comparing actively and passively pitching tails over a wide range of Strouhal frequency, inertia, damping ratio, and Reynolds numbers. The results reveal a consistent performance trade-off: configurations that generate larger thrust tend to operate at lower power ratios, while those that exhibit higher power ratios generally produce reduced thrust. Actively pitching tails outperform passive ones in thrust generation, particularly at the higher Reynolds number, whereas passively pitching tails can achieve a superior power ratio at lower Reynolds numbers. The behavior is strongly conditioned by how large the pitching amplitudes are. Increased amplitudes arising from higher Strouhal frequency

improve performance, while those produced by smaller inertia or looser joints may be detrimental. These outcomes suggest that smaller swimmers may benefit from passive pitching, whereas larger swimmers are more likely to rely on active pitching for optimal propulsion.

The second study extends this understanding into three dimensions by introducing non-linear tunable stiffness at the peduncle. Unlike the linear torsional stiffness explored in Chapter. 2.3.2, the stiffness here varies with displacement, enabling the caudal fin to undergo large angular excursions while remaining mechanically stable. This gives rise to a natural recoil response in which the rapidly increasing restoring moment near the extremes of motion accelerates the fin back toward its neutral position. The resulting amplification of pitching and the associated phase shift relative to the heaving emerge. This nonlinear recoil substantially alters the three-dimensional vortex dynamics, promoting the formation of coherent ring-like and hairpin-like vortices and producing a more prominent downstream momentum jet.

Together, these two studies demonstrate that passive pitching is not a singular phenomenon but a spectrum governed by inertia, dampidamping rationg-ratio, Reynolds number, and, crucially, stiffness characteristics. The two-dimensional results show how linear passive joints can support efficient locomotion under certain conditions, while the three-dimensional simulations reveal how nonlinear stiffness can transform the fin into a self-regulating, hydrodynamically advantageous propulsor capable of generating amplified pitching alongside coherent vortex shedding. By situating linear and nonlinear passive dynamics within a unified framework, this thesis highlights the central role of stiffness modulation, whether constant or displacement-dependent in controlling amplitude, phase, and wake structure.

Overall, the combined findings indicate that passive synchronization, when paired with the right stiffness, can enable swimmers to achieve propulsion comparable to, and even better than,

actively pitching configurations. This insight not only clarifies the mechanical and hydrodynamic basis of biological peduncles but also provides guiding principles for the design of future bio-inspired propulsion systems in which structural tuning reduces the need for active pitching while maintaining strong and sustained thrust production.

4.3 Recommendations for Future Work

The following directions are recommended for future investigations into swimmers equipped with passively pitching caudal fins.

Numerical investigations

1. **Fish schooling**: The influence of nonlinear peduncle stiffness on caudal-fin dynamics can be extended to multi-swimmer configurations. Studying two or more swimmers in tandem or parallel formation would help clarify how passive pitching behaves in collective hydrodynamics and wake–wake interactions.

2. **Fully passive caudal fin**: A swimmer whose caudal fin is allowed to both heave and pitch freely—without prescribed kinematics—could be developed to deepen understanding of the vortex dynamics governing fully passive body–fin systems.

3. **Flexible swimming body**: The trunk and caudal fin may be modeled as a continuous flexible structure with tunable material properties. Such a formulation would allow exploration of how fish-like bodies adapt their kinematics in response to environmental changes, with direct implications for the design of next-generation AUVs.

4. **Scaling laws**: Introducing scaling relationships for thrust, efficiency, and cost of transport

would enable a more comprehensive assessment of performance across swimmer size, stiffness, and Reynolds number regimes.

Experimental investigations

Robot with nonlinear adaptive stiffness: A robotic swimmer incorporating a caudal fin with passively pitching motion and nonlinear adaptive stiffness could be developed to validate the numerical findings and provide further insight into the role of passive pitching in bio-inspired propulsion.

Bibliography

[1] Amy Gao and Michael S Triantafyllou. Independent caudal fin actuation enables high energy extraction and control in two-dimensional fish-like group swimming. *Journal of Fluid Mechanics*, 850:304–335, 2018.

[2] Robin Thandiackal and George Lauder. In-line swimming dynamics revealed by fish interacting with a robotic mechanism. *elife*, 12:e81392, 2023.

[3] Christopher J Esposito, James L Tangorra, Brooke E Flammang, and George V Lauder. A robotic fish caudal fin: effects of stiffness and motor program on locomotor performance. *Journal of Experimental Biology*, 215(1):56–67, 2012.

[4] Brooke E Flammang, George V Lauder, Daniel R Troolin, and Tyson E Strand. Volumetric imaging of fish locomotion. *Biology letters*, 7(5):695–698, 2011.

[5] Stefano Marras and Maurizio Porfiri. Fish and robots swimming together: attraction towards the robot demands biomimetic locomotion. *Journal of The Royal Society Interface*, 9(73):1856–1868, 2012.

[6] Haibo Dong, Longfei Li, and Arvind Santhanakrishnan. Understanding energy saving strate-

gies in trout swimming using volumetric piv. *Proceedings of the National Academy of Sciences*, 118(3):e2016706118, 2021.

[7] Tingyu Ming, Bowen Jin, Jialei Song, Haoxiang Luo, Ruxu Du, and Yang Ding. 3d computational models explain muscle activation patterns and energetic functions of internal structures in fish swimming. *PLoS computational biology*, 15(9):e1006883, 2019.

[8] Amirhossein Fardi, Hamayun Farooq, Imran Akhtar, Arman Hemmati, and Muhammad Saif Ullah Khalid. Characterizing the role of hind flippers in hydrodynamics of a harbor seal. *Bioinspiration & Biomimetics*, 20(4):046010, 2025.

[9] Kathryn J Mengerink, Cindy L Van Dover, Jeff Ardron, Maria Baker, Elva Escobar-Briones, Kristina Gjerde, J Anthony Koslow, Eva Ramirez-Llodra, Ana Lara-Lopez, Dale Squires, et al. A call for deep-ocean stewardship. *Science*, 344(6185):696–698, 2014.

[10] P Amal, Arjun R Nair, H Arunav, Rithu Raj, VM Akhil, Charbel Tawk, and Karthik V Shankar. Bioinspiration and biomimetics in marine robotics: a review on current applications and future trends. *Bioinspiration & Biomimetics*, 2024.

[11] Daniele Costa, Matteo Franciolini, Giacomo Palmieri, Andrea Crivellini, and David Scaradozzi. Computational fluid dynamics analysis and design of an ostraciiform swimming robot. In *2017 IEEE International Conference on Robotics and Biomimetics (ROBIO)*, pages 135–140. IEEE, 2017.

[12] Yufeng Chen, Hongqiang Wang, E Farrell Helbling, Noah T Jafferis, Raphael Zufferey, Aaron Ong, Kevin Ma, Nicholas Gravish, Pakpong Chirarattananon, Mirko Kovac, et al.

A biologically inspired, flapping-wing, hybrid aerial-aquatic microrobot. *Science robotics*, 2(11):eaao5619, 2017.

[13] Maham Kamran, Amirhossein Fardi, Chengyu Li, and Muhammad Saif Ullah Khalid. How does vortex dynamics help undulating bodies spread odor? *Physics of Fluids*, 36(11), 2024.

[14] Yi Zhu, Fang-Bao Tian, John Young, James C Liao, and Joseph CS Lai. A numerical study of fish adaption behaviors in complex environments with a deep reinforcement learning and immersed boundary–lattice boltzmann method. *Scientific Reports*, 11(1):1691, 2021.

[15] George V Lauder. Function of the caudal fin during locomotion in fishes: kinematics, flow visualization, and evolutionary patterns. *American Zoologist*, 40(1):101–122, 2000.

[16] Haotian Hang, Sina Heydari, John H Costello, and Eva Kanso. Active tail flexion in concert with passive hydrodynamic forces improves swimming speed and efficiency. *Journal of Fluid Mechanics*, 932:A35, 2022.

[17] Imran Akhtar, Rajat Mittal, George V. Lauder, and Peter Madden. Hydrodynamics of a biologically inspired tandem flapping foil configuration. *Theoretical and Computational Fluid Dynamics*, 21:155–170, 2007.

[18] Richard Knoller. Die gesetzedes luftwiderstandes. *Flug-und Motortechnik (Wien)*, 3(21):1–7, 1909.

[19] Albert Betz. Ein beitrag zur erklaerung segelfluges. *Z Flugtech Motorluftschiffahrt*, 3:269–272, 1912.

[20] Michael S Triantafyllou and George S Triantafyllou. An efficient swimming machine. *Scientific american*, 272(3):64–70, 1995.

[21] Michael James Lighthill. Aquatic animal propulsion of high hydromechanical efficiency. *Journal of Fluid Mechanics*, 44(2):265–301, 1970.

[22] George V Lauder, Brooke Flammang, and Silas Alben. Passive robotic models of propulsion by the bodies and caudal fins of fish, 2012.

[23] Kara L Feilich and George V Lauder. Passive mechanical models of fish caudal fins: effects of shape and stiffness on self-propulsion. *Bioinspiration & biomimetics*, 10(3):036002, 2015.

[24] Samuel Haedong Kim, Heuiseok Kang, Kyungtae Kang, Sang Ho Lee, Kwan Hyun Cho, and Jun Young Hwang. Effect of meniscus damping ratio on drop-on-demand electrohydrodynamic jetting. *Applied Sciences*, 8(2):164, 2018.

[25] Geng Liu, Biao Geng, Xudong Zheng, Qian Xue, Haibo Dong, and George V Lauder. An image-guided computational approach to inversely determine in vivo material properties and model flow-structure interactions of fish fins. *Journal of Computational Physics*, 392:578–593, 2019.

[26] Frank E Fish and George V Lauder. Control surfaces of aquatic vertebrates: active and passive design and function. *Journal of Experimental Biology*, 220(23):4351–4363, 2017.

[27] Sanaz Bazaz Behbahani and Xiaobo Tan. Design and modeling of flexible passive rowing joint for robotic fish pectoral fins. *IEEE Transactions on Robotics*, 32(5):1119–1132, 2016.

[28] Changlin Qiu, Zhengxing Wu, Jian Wang, Min Tan, and Junzhi Yu. Locomotion optimization

of a tendon-driven robotic fish with variable passive tail fin. *IEEE Transactions on Industrial Electronics*, 70(5):4983–4992, 2022.

[29] Di Chen, Zhengxing Wu, Huijie Dong, Min Tan, and Junzhi Yu. Exploration of swimming performance for a biomimetic multi-joint robotic fish with a compliant passive joint. *Bioinspiration & Biomimetics*, 16(2):026007, 2020.

[30] Qixin Wang, Jianran Zhang, Peiqi Huang, and Yong Zhong. Design and modeling of a robotic fish with modular adaptive variable stiffness passive joint. *IEEE/ASME Transactions on Mechatronics*, 2025.

[31] Yang Lu, Shaomin Meng, Cheng Xing, Yiwei Hao, Yonghui Cao, Guang Pan, and Yong Cao. Effect of active–passive deformation on the thrust by the pectoral fins of bionic manta robot. *Journal of Bionic Engineering*, 21(2):718–728, 2024.

[32] Yiming Lu, Haicheng Zhang, Daolin Xu, and Wei-Xi Huang. Nonlinear tunable stiffness for high-efficiency biomimetic propulsion. *Journal of Fluid Mechanics*, 1017:A7, 2025.

[33] Michel Bergmann, Angelo Iollo, and Rajat Mittal. Effect of caudal fin flexibility on the propulsive efficiency of a fish-like swimmer. *Bioinspiration & biomimetics*, 9(4):046001, 2014.

[34] Muhammad Saif Ullah Khalid, Junshi Wang, Haibo Dong, and Moubin Liu. Flow transitions and mapping for undulating swimmers. *Physical Review Fluids*, 5(6):063104, 2020.

[35] Muhammad Saif Ullah Khalid, Junshi Wang, Imran Akhtar, Haibo Dong, Moubin Liu, and Arman Hemmati. Larger wavelengths suit hydrodynamics of carangiform swimmers. *Physical Review Fluids*, 6(7):073101, 2021.

[36] Muhammad Saif Ullah Khalid, Imran Akhtar, and Haibo Dong. Hydrodynamics of a tandem fish school with asynchronous undulation of individuals. *Journal of Fluids and Structures*, 66:19–35, 2016.

[37] Seshadri Sridhar, Ali H Nayfeh, and Dean T Mook. Nonlinear resonances in a class of multi-degree-of-freedom systems. *The Journal of the Acoustical Society of America*, 58(1):113–123, 1975.

[38] Seung-Jin Baek, Sang Bong Lee, and Hyung Jin Sung. Response of a circular cylinder wake to superharmonic excitation. *Journal of Fluid mechanics*, 442:67–88, 2001.

[39] Geng Liu, Yan Ren, Haibo Dong, Otar Akanyeti, James C Liao, and George V Lauder. Computational analysis of vortex dynamics and performance enhancement due to body–fin and fin–fin interactions in fish-like locomotion. *Journal of fluid mechanics*, 829:65–88, 2017.

[40] Hrvoje Jasak. Dynamic mesh handling in openfoam. In *47th AIAA aerospace sciences meeting including the new horizons forum and aerospace exposition*, page 341, 2009.

[41] Dev Pradeepkumar Nayak, Ali Tarokh, and Muhammad Saif Ullah Khalid. Comparative investigations on active and passive tails of undulating swimmers. *arXiv preprint arXiv:2511.03057*, 2025.

[42] Kelsey N Lucas, George V Lauder, and Eric D Tytell. Airfoil-like mechanics generate thrust on the anterior body of swimming fishes. *Proceedings of the National Academy of Sciences*, 117(19):10585–10592, 2020.

[43] Maxime Picard-Deland, Mathieu Olivier, Guy Dumas, and Thomas Kinsey. Oscillating-foil turbine operating at large heaving amplitudes. *AIAA Journal*, 57(12):5104–5113, 2019.

[44] Jie Wu, Chang Shu, N Zhao, and F-B Tian. Numerical study on the power extraction performance of a flapping foil with a flexible tail. *Physics of Fluids*, 27(1), 2015.

[45] Ramiro Godoy-Diana, Catherine Marais, Jean-Luc Aider, and José Eduardo Wesfreid. A model for the symmetry breaking of the reverse bénard–von kármán vortex street produced by a flapping foil. *Journal of Fluid Mechanics*, 622:23–32, 2009.

[46] Imran Akhtar and Rajat Mittal. A biologically inspired computational study of flow past tandem flapping foils. In *35th AIAA Fluid Dynamics Conference and Exhibit*, page 4760, 2005.

[47] Haibo Dong, M. Bozkurttas, Rajat Mittal, F. M. Najjar, B. Marelli, and George V. Lauder. Wake topology and hydrodynamic performance of low-aspect-ratio flapping foils. *Journal of Fluid Mechanics*, 566:309–343, 2006.